Role of torsional potential in chain conformation, thermodynamics, and glass formation of simulated polybutadiene melts

F. Demydiuk, M. Solar, H. Meyer, O. Benzerara, W. Paul, J. Baschnagel

Role of torsional potential in chain conformation, thermodynamics and glass formation of simulated polybutadiene melts

F. Demydiuk,[1] M. Solar,[1] H. Meyer,[1] O. Benzerara,[1] W. Paul,[2] and J. Baschnagel[1,*]

[1] *Université de Strasbourg, CNRS, Institut Charles Sadron UPR 22, F-67000 Strasbourg, France*
[2] *Martin Luther Universität, Institut für Physik, D-06099 Halle, Germany*

(Dated: May 12, 2022)

For polymer chains the torsional potential is an important intramolecular energy influencing chain flexibility and segmental dynamics. Through molecular dynamics simulations of an atomistic model for melts of *cis-trans* 1,4-polybutadiene (PBD) we explore the effect of the torsions on conformational properties (bond vector correlations, mean-square internal distances), fundamental thermodynamic quantities (density, compressibility, internal energy, specific heat), and glass transition temperature T_g. This is achieved by systematically reducing the strength of the torsional potential, starting from the chemically realistic chain (CRC) model with full potential towards the freely rotating chain (FRC) model without torsional potential. For the equilibrium liquid we find that the effect of the torsions on polymer conformations is very weak. Still weaker is the influence on the monomer density ρ and isothermal compressibility κ_T of the polymer liquid, both of which can be considered as independent of the torsional potential. We show that a van–der–Waals-like model proposed by Long and Lequeux [Eur. Phys. J. E **4**, 371 (2001)] allows to describe very well the temperature (T) dependence of ρ and κ_T. We also find that our data obey the linear relation between $1/\sqrt{k_B T \rho \kappa_T}$ and $1/T$ (with the Boltzmann constant k_B) that has recently been predicted and verified on experiment by Schweizer and coworkers [J. Chem. Phys. **140**, 194507 (2014)]. For the equilibrium liquid the simulations result in a specific heat, at constant pressure and at constant volume, which increases on cooling. This T dependence is opposite to the one found experimentally for many polymer liquids, including PBD. We suggest that this difference between simulation and experiment may be attributed to quantum effects due to hydrogen atoms and backbone vibrations which, by construction, are not included in the classical united-atom model employed here. Finally, we also determine T_g from the density-temperature curve monitored in a finite-rate cooling process. While the influence of the torsional potential on $\rho(T)$ is vanishingly small in the equilibrium liquid, the effect of the torsions on T_g is large. We find that T_g decreases by about 150 K when going from the CRC to the FRC model.

I. INTRODUCTION

The drastic increase of the structural relaxation time by many orders of magnitude is a basic characteristic observed when cooling glass-forming liquids [1, 2], including polymer melts [1, 3], toward low temperature. For polymers the structural relaxation is related to the local segmental dynamics which are determined by intramolecular conformational energies (bonding and bending energies, relative energy of stable conformations and barriers between them, etc.) and nonbonded excluded volume and cohesive energies [4, 5]. The importance of intramolecular and nonbonded interactions for polymer glass formation has long been appreciated by the polymer science community [5, 6], and both factors are explicitly incorporated into current developing coarse-grained theories for glass-forming polymers, such as the generalized entropy theory [7, 8] or the elastically collective nonlinear Langevin equation theory [9–11].

A complete, microscopic description of polymer liquids can be obtained by molecular dynamics (MD) simulations that integrate the classical equations of motion for model systems and enable the study of the equilibrium structure and dynamics [4, 5, 7, 8, 12, 13] up to time scales of microseconds on modern-day processors and aided by efficient simulation strategies [14]. Such simulations allow to single out the role of intramolecular or nonbonded interactions by systematically varying the strength of the respective potential while keeping the other potentials unchanged. For bead-spring models, recent examples involve the variation of cohesive energy via the depth of the nonbonded potential well [7], or of chain stiffness via the amplitude of the bond-angle potential [15]. As a general finding, the simulations show that for fully flexible models without bond-angle potential, changes in the temperature (T) dependence of the structural relaxation time caused by cohesive energy strength can be largely eliminated when scaling T with the nonbonded potential-well depth, while this is not possible for models with strong bond-angle potential [7]. Moreover, increase of chain stiffness, at fixed cohesive energy strength, shifts the glassy dynamics to higher temperature. These findings are in general accord with the results of an earlier systematic simulation study for a bead-spring model [16–18], lucidly reviewed in Ref. [5], where chain stiffness is varied not only by the bond-angle potential but also by the torsional potential.

Torsional potentials are invariably a part of the force field for atomistic polymer models. Work on a chemically realistic united-atom model for polybutadiene (PBD) [4]

* Corresponding author: jorg.baschnagel@ics-cnrs.unistra.fr

varied the torsional potentials [19–22] and reported a remarkable feature. Complete elimination of the torsional potentials does not change the structure of the liquid or of the polymers, and so chain stiffness [19], whereas the structural relaxation is significantly enhanced compared to the underlying parent model with full torsional potential [19–22]. Although this relation between the torsional potentials and melt properties might be specific to the PBD model employed, it hints at the interesting possibility to separate structural and dynamic effects. According to the rotational isomeric state model [23], the equilibrium polymer structure is determined by the population of the minima of the torsional potential. Exploration of the torsional energy landscape, however, requires to cross the energy barriers between the minima. Developing models that maintain the minima but reduce the barriers could be of great interest: on the one hand, as a speed-up algorithm to accelerate the segmental dynamics, thereby enabling equilibration at low T where standard MD simulations of the model with full torsions would be impractical; on the other hand, as a tool to explore the fundamental question of how to incorporate intramolecular barriers in the construction of increasingly accurate microscopic theories of vitrification in polymer liquids.

In this paper we make a very first step in this direction by revisiting and extending the work on the PBD models discussed in Refs. [19–22]. The layout of the paper is as follows. In Sec. II, we describe the atomistic polymer model, introduce variants with reduced or eliminated torsional potentials, and outline the simulation methodology. This presentation is quite detailed for the purpose of later reference. Subsequently, we discuss the impact of the torsional potential on polymer conformation in Sec. III, on density and compressibility in Sec. IV, and on internal energy and specific heat in Sec. V. Much of this discussion refers to the equilibrium liquid. Nonequilibrium properties induced by finite-rate cooling processes are illustrated in Sec. III by the shift of the glass transition temperature with reduction of the torsional potential. We summarize and discuss our main results in Sec. VI. Further supporting information is given in the Supplementary Material.

II. MODEL AND SIMULATION

A. Atomistic model of 1,4 polybutadiene

We examine a polymer melt with $N_c = 40$ chains of 1,4-polybutadiene (PBD). Each PBD chain (CH_2–CH=CH–CH_2)$_n$ consists of $N_m = 29$ monomers which can adopt a *trans* or a *cis* configuration (Fig. 1). Our PBD chains are random copolymers with 55% *trans* and 45% *cis* monomers. The chemical structure of PBD is not explicitly taken into account, but CH_2 and CH are modeled as particles, i.e. as united atoms (UAs), with mass $m_{CH_2} = 14.027\,\mathrm{g/mol}$ and $m_{CH} = 13.019\,\mathrm{g/mol}$ [25], implying that a monomer has the mass $M_0 = 54.092\,\mathrm{g/mol}$. With $N_m = 29$ a chain comprises $N = 116$ UAs and the melt has $N_c N = 4640$ particles in total.

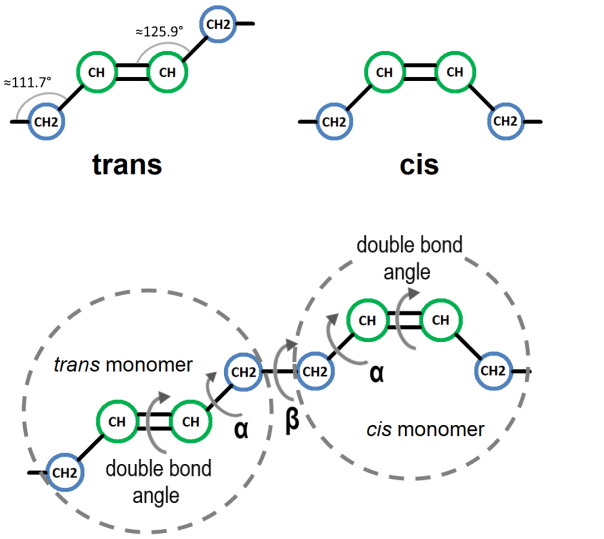

FIG. 1. Top sketch: *trans* and *cis* configuration of a monomer in PBD. For the *trans* monomer the values of the bond angles from Table II are indicated. The *cis* monomer has the same angles. Bottom sketch: Torsion (or dihedral) angles of PBD for double bonds, α *trans* and α *cis* bonds, and β bonds. The naming of the angles follows Ref. [24].

Our simulation model for PBD builds upon a quantum chemistry based united atom potential [24, 26] that predicts static [24, 26] and dynamic [27–30] properties of a PBD melt in very good agreement with experiment over a wide range of temperatures (cf. [4] for a review). Recent work with this model has focused on polymer films [31–35] and employed an adapted version of the original potential functions [24, 26] for implementation in the GROMACS code [36]. Since we modify some of the interaction potentials here, we review the force field utilized in [31–35] and explain the changes made.

The force field of PBD is composed of four potentials associated with bond stretching, bond-angle bending, torsional rotations, and pair interactions. Stretching of the bond length ℓ is modeled by a harmonic potential

$$U_{\mathrm{bond}}(\ell) = K_{\mathrm{bond}}(\ell - \ell_0)^2 \,, \qquad (1)$$

where K_{bond} is (half of) the force constant and ℓ_0 the equilibrium bond length. PBD has three different bonds.

TABLE I. Parameters for the bond potential of Eq. (1).

Bond length type	K_{bond} (kcal/(mol Å^2))	ℓ_0 (Å)
CH=CH	2500	1.34
CH_2–CH_2	2500	1.53
CH–CH_2	2500	1.50

The corresponding values for ℓ_0 are taken from Ref. [24] and given in Table I. Prior work [4, 19, 22, 24, 26, 29–35, 37] has not used Eq. (1), but fixed ℓ at its equilibrium value. Here we are changing the bond potential because the simulations are carried out with the LAMMPS code [38]. To assure good parallel performance the backbone bonds of PBD cannot be constrained in LAMMPS, contrary to GROMACS. Since we want to stay close to the original model with $\ell = \ell_0$, we limit the bond length fluctuations by choosing a large value for the force constant, $K_{\rm bond} = 2500\,{\rm kcal/mol\,\AA}^2$ (cf. Table I). This value is a compromise between spectroscopic data [39] and not too long computation times (see Sec. II C). With this value one finds $\sqrt{\langle(\ell-\ell_0)^2\rangle} = \sqrt{k_{\rm B}T/(2K_{\rm bond})} \approx 0.01$ Å for $T = 353\,{\rm K}$, the highest temperature studied in the following. Thus, bond length fluctuations are less than 1% of ℓ_0.

In the simulation the bond angle θ is calculated by the scalar product of the bond vectors. Computationally, it is therefore convenient to express the bending potential in terms of $\cos\theta$. Here the bending potential is taken to be harmonic in $\cos\theta$,

$$U_{\rm ang}(\theta) = K_{\rm bend}(\cos\theta - \cos\theta_0)^2 \;, \tag{2}$$

whereas the original model of Ref. [24] employed

$$U_{\rm ang}(\theta) = \frac{1}{2}\,k_\theta(\theta-\theta_0)^2 \;.$$

Assuming θ to be close to the equilibrium bond angle θ_0 the bending stiffnesses $K_{\rm bend}$ and k_θ are related to one another by [40]

$$K_{\rm bend} = \frac{k_\theta}{2\sin^2\theta_0} \;. \tag{3}$$

In this way, $K_{\rm bend}$ was determined from k_θ of Ref. [24]. As indicated in Fig. 1, PBD has two different bond angles. The corresponding values for θ_0 and $K_{\rm bend}$ are given in Table II. $K_{\rm bend}$ is smaller than $K_{\rm bond}$ by a factor of about 37, implying larger fluctuations of θ than for ℓ. Still, the fluctuations remain very small because $\sqrt{\langle(\theta-\theta_0)^2\rangle} \approx [k_{\rm B}T/(2K_{\rm bend}\sin^2\theta_0)]^{1/2} \approx 4.6°$ even for $T = 353\,{\rm K}$

The torsion (or dihedral) angle ϕ is the angle between two intersecting planes defined by three successive bonds along the chain backbone. The associated potential $U_{\rm tor}(\phi)$ accounts for steric interactions between UAs separated by these three bonds. Since $U_{\rm tor}(\phi)$ is an even and periodic function of ϕ, it can be expressed

TABLE II. Parameters for the bending potential of Eq. (2).

Bond angle type	$K_{\rm bend}$ (kcal/mol)	θ_0 (deg)
CH_2–CH–CH	68.1475	125.896
CH–CH_2–CH_2	66.5925	111.652

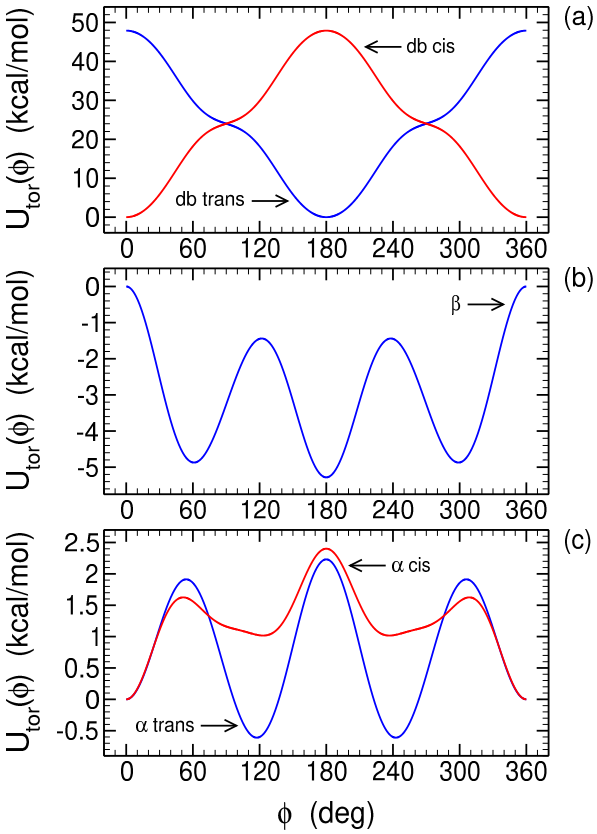

FIG. 2. Torsional potential $U_{\rm tor}(\phi)$ (in kcal/mol) for the different torsion angles ϕ illustrated in Fig. 1: in panel (a) for the double bonds of the *cis* (db *cis*) and *trans* (db *trans*) configuration of a monomer, in panel (b) for the β bond between two monomers, and in panel (c) for the α bond adjacent to the double bond of a *cis* (α *cis*) and *trans* (α *trans*) configuration.

as an expansion in powers of $\cos\phi$. Here we employ the Ryckaert–Bellemans function [41],

$$U_{\rm tor}(\phi) = \sum_{n=1}^{6} A_n(\cos\phi)^{n-1} \;, \tag{4}$$

while the original model of Refs. [24, 26] utilized

$$U_{\rm tor}(\phi) = \frac{1}{2}\sum_{n=1}^{6} k_n\,[1-\cos(n\phi)] \;. \tag{5}$$

In these equations ϕ is in the interval $0° \le \phi \le 360°$ and A_n and k_n are energy coefficients. The A_n were determined by adjusting the Ryckaert–Bellemans function to Eq. (5) [42]. The corresponding $\{A_n\}_{n=1,\ldots,6}$ are given in Table III for the five different torsion angles depicted in Fig. 2.

Figure 2(a) plots Eq. (4) for the double bond of the *cis* and *trans* monomer. Per definition, the minimum occurs at $\phi_{\rm min} = 0°$ (or 360°) for *cis* and at $\phi_{\rm min} = 180°$ for *trans*. Deviations from these planar configurations are

TABLE III. Coefficients A_n (in kcal/mol) of the torsional potential (4) for the different dihedrals of PBD indicated in Fig. 1.

torsion angle	A_1	A_2	A_3	A_4	A_5	A_6
double bond (*cis*)	24.011	−5.31647	0.100537	−27.5485	−0.160949	8.91436
double bond (*trans*)	24.011	5.31647	0.100537	27.5485	−0.160949	−8.91436
β	−3.2615	−4.94228	0.340155	5.58258	0.280129	2.00093
α (*cis*)	1.16054	0.360163	0.680313	1.48069	−0.640294	−3.04142
α (*trans*)	0.385179	3.46661	1.05049	−3.86178	−0.320148	−0.720332

possible, but quickly become penalized energetically due to large values of $U_{\rm tor}(\phi)$ relative to the thermal energy that is $k_{\rm B}T \simeq 0.7\,$kcal/mol at $T = 353\,$K [43]. The potential energy of the inflection points at $\phi = 90°, 270°$ corresponds to about 12 000 K and that of the maxima at $\phi = 180°$ for *cis* or $\phi = 0°, 360°$ for *trans* to about 24 000 K. These temperatures are much larger than the temperatures studied ($T \leq 353\,$K) so that the corresponding angles are never adopted in the simulation. In practice, the double bonds stay close to the planar equilibrium state. We can estimate typical fluctuations around this state by a harmonic expansion of $U_{\rm tor}(\phi)$ around $\phi_{\rm min}$. This expansion provides an excellent approximation up to $U_{\rm tor}(\phi \approx \phi_{\rm min} \pm 20°) \approx 2.7\,$kcal/mol with a force constant $k_\phi = 0.0133\,\text{kcal}/(\text{mol}\,\text{deg}^2)$, implying that $\sqrt{\langle(\phi - \phi_{\rm min})^2\rangle} = \sqrt{k_{\rm B}T/k_\phi} \approx 7°$ for $T = 353\,$K. Deviations from the equilibrium state are therefore small, though larger than for ℓ and θ. The double bonds, together with the bond lengths and bond angles, are therefore stiff degrees of freedom.

The main source of chain flexibility and conformational rearrangements in PBD stems from torsional rotations around the β bond and the α *cis* and α *trans* bonds. This is the case because the maximum potential energy of these dihedrals is an order of magnitude smaller than for the double bonds, as seen from Fig. 2(b) and (c). Figure 2(b) plots Eq. (4) for the β bond. The torsional energy of this bond has the shape familiar from hydrocarbon chains, such as polyethylene [44]. There are three minima, the primary minimum being the *trans* state at $\phi = 180°$ and the secondary minima being the *gauche-plus* and *gauche-minus* states at $\phi \simeq 180° \pm 120°$. The energy difference between *trans* and *gauche* states is about $0.41\,\text{kcal/mol} \approx 0.58 k_{\rm B}T$ at 353 K and the barrier at $\phi \simeq 180° \pm 60°$ is about $3.84\,\text{kcal/mol} \approx 5.48 k_{\rm B}T$ at 353 K. Figure 2(b) plots Eq. (4) for the α *cis* and α *trans* bonds. Qualitatively, the shape of $U_{\rm tor}(\phi)$ for these dihedrals is the mirror image of $U_{\rm tor}(\phi)$ of the β bond, having minima at $\phi = 0°, 360°$ and $\phi \simeq 180° \pm 60°$. The barriers between these minima are smaller than those of the β bond, implying that torsional transitions are more easily possible about the highly flexible dihedals.

Pair interactions between united atoms of a chain separated by four or more bonds and between united atoms of different chains are modeled by a 12-6 Lennard–Jones (LJ) potential with an additional switching function $S(r)$ commonly used in the GROMACS code [36] and also implemented in LAMMPS (see pair_style lj/gromacs command [38]),

$$U_{\rm pair}(r) = \begin{cases} 4\epsilon\left[\left(\frac{\sigma}{r}\right)^{12} - \left(\frac{\sigma}{r}\right)^{6}\right] + S(r) & \text{if } r < r_{\rm c}\,, \\ 0 & \text{if } r \geq r_{\rm c}\,. \end{cases} \quad (6)$$

The switching function $S(r)$ shifts $U_{\rm pair}(r)$ smoothly to zero between an inner cutoff r_1 and the outer cutoff $r_{\rm c}$ so that the force and second derivative of $U_{\rm pair}(r)$ vanish continuously at $r_{\rm c}$ [42]. We choose constant values, $r_1 =$ 9 Å and $r_{\rm c} =$ 12 Å, for all pairs of UAs. The original model [4, 19, 22, 24, 26, 29–35, 37] did not apply $S(r)$, but employed an LJ-potential truncated at $r_{\rm c} = 9$ Å with tail corrections [45] for energy and pressure. Here we change the pair interaction to Eq. (6) to avoid impulsive corrections [45, 46] and to allow for future extension to polymer films where the isotropic tail corrections cannot be applied. However, the original model was validated against experiments [24, 26–30], a salient feature we want to keep. To achieve this we take the same values for the LJ diameters σ_{ij} ($i, j = \text{CH}_2, \text{CH}$) as in Ref. [24] but enhance the values of the LJ energies ϵ_{ij} so that the monomer density of the model with enhanced ϵ_{ij} is the same as for the original model with tail corrections [42]. The resulting LJ parameters are summarized in Table IV.

The values of σ_{ij} show that the inner cutoff r_1 is $r_1 > 2\sigma_{ij}$ and the outer cutoff $r_{\rm c}$ is $r_{\rm c} \gtrsim 3\sigma_{ij}$. Therefore, the distance $r_{\rm c} - r_1$ (= 3 Å) over which $S(r)$ smooths $U_{\rm pair}(r)$ to zero is close to about one particle diameter.

From the point of view of the pair interactions PBD corresponds to a binary mixture. The values in Table IV show that PBD deviates from the standard Lorentz–Berthelot mixing rule [47]. By contrast to the Lorentz rule, PBD is a nonadditive mixture, since $\sigma_{ij} \neq (\sigma_{ii} + \sigma_{jj})/2$, and has enhanced mixing ability relative to the Berthelot rule because $\epsilon_{ij} > \sqrt{\epsilon_{ii}\epsilon_{jj}}$ [42]. In simple liquids and metallic alloys both features are favorable for better glass-forming ability [48, 49]. We discuss this point further in the Supplementary Material by comparing the

TABLE IV. Parameters of the Lennard–Jones potential (6) for the different types of united atoms $i, j = \text{CH}_2, \text{CH}$.

Pair type	ϵ_{ij} (kcal/mol)	σ_{ij} (Å)
$\text{CH}_2 \leftrightarrow \text{CH}_2$	0.107639	4.00904
$\text{CH} \leftrightarrow \text{CH}$	0.114999	3.38542
$\text{CH}_2 \leftrightarrow \text{CH}$	0.116723	3.79256

LJ parameters of PBD with those of the Kob–Andersen binary mixture [50–52].

B. Model variants with reduced torsional potential

In the following we refer to the PBD model described in Sec. II A as the chemically realistic chain (CRC) model. To explore the impact of the dihedrals on the properties of PBD we also study model variants with reduced torsional potential while keeping the other potentials for the bond lengths, bond angles and pair interactions unchanged. These variants are obtained by replacing $U_{\rm tor}(\phi)$ for all dihedral angles with $\lambda U_{\rm tor}(\phi)$ where $\lambda = 0, 1/4, 1/2$. We refer to these models as:

$$\begin{aligned} \lambda &= 0: && \text{freely rotating chain (FRC) model ,} \\ \lambda &= \tfrac{1}{4}: && \text{CRC4 model ,} \\ \lambda &= \tfrac{1}{2}: && \text{CRC2 model ,} \\ \lambda &= 1: && \text{CRC model .} \end{aligned} \tag{7}$$

The FRC model has already been introduced and studied in Refs. [19, 20]. Due to the absence of the torsional potential the model enables free rotation around the double bonds, thereby eliminating the difference between *cis* and *trans* conformers. Within the FRC model PBD is therefore no longer a random copolymer of *cis* and *trans* monomers, but a homopolymer. While it would have been possible to preserve the copolymer character by maintaining the dihedral potentials for the double bonds only [22], we adopted the FRC model here because it resembles extensively studied glass-forming bead–spring models with intramolecular forces resulting only from bond-length and bending potentials (see e.g. [5, 7, 13, 17, 18, 53, 54]. The CRC4 and CRC2 models are introduced because they smoothly interpolate between the FRC and CRC models.

C. Simulation methodology

We perform molecular dynamics (MD) simulations of PBD with the LAMMPS code [38, 55]. The classical equations of motion are integrated by the rRESPA multi-timescale integrator with two hierarchical levels: The outer level integrates the pair interactions with a time step $\delta t_{\rm outer} = 1$ fs, while the inner level integrates the bond-length, bending and dihedral potentials with a four times smaller time step $\delta t_{\rm inner} = 0.25$ fs. With the estimates of the bond oscillation time $\tau_{\rm bond} \approx 1.6 \times 10^{-14}$ s and of the LJ time $\tau_{\rm LJ} \approx 1.8 \times 10^{-12}$ s [56] these choices imply that the time steps are much smaller than the time scales of the associated potentials ($\delta t_{\rm inner}/\tau_{\rm bond} \approx 1.6\times10^{-2}$, $\delta t_{\rm outer}/\tau_{\rm LJ} \approx 5.6\times10^{-4}$). We combine the rRESPA integrator with the Nosé–Hoover thermostat and the Nosé–Hoover–Andersen barostat to control temperature T and pressure p in NPT simulations and with the Nosé–Hoover thermostat when carrying out canonical NVT simulations at constant volume V (LAMMPS parameters [38]: Tdamp = 1000 fs, Tchain = 3; Pdamp = 10000 fs, Pchain = 3). All simulations make use of periodic boundary conditions.

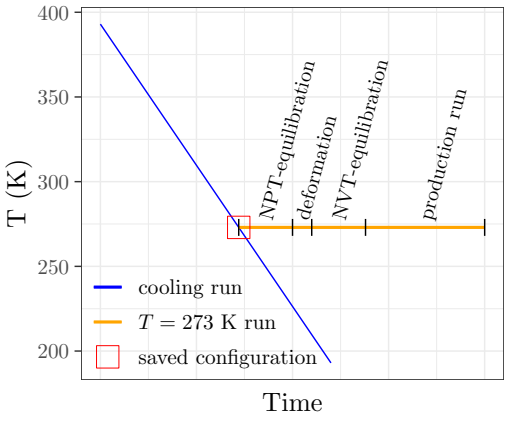

FIG. 3. Sketch of the simulation protocol consisting a cooling run according to Eq. (8) followed by equilibration and production runs. Starting from the melt configuration stored during the cooling run at a given T (here $T = 273$ K), equilibration comprises three steps: 1) NPT relaxation over 100 ns with determination of the equilibrium volume $V(T)$ as the time average over the final part of the time series of the volume, 2) the instantaneous volume of the final configuration of the NPT run is rapidly deformed over 10 ps toward $V(T)$, 3) NVT relaxation at $V(T)$ over another 100 ns. Equilibration is followed by a production run which lasts 1 μs or more, depending on temperature.

The simulations are started from an equilibrated melt configuration of the CRC model at $T = 353$ K taken from Ref. [34]. This configuration is further equilibrated under NPT conditions to impose a pressure of $p = 0$ atm. This pressure was chosen because future work will focus on supported polymer films where the films are in contact with vacuum at its free surface. For these studies bulk simulations at $p = 0$ atm serve as a reference point. Starting from $T_{\rm i} = 353$ K the melt is continuously cooled down to $T = 3$ K at $p = 0$ atm according to the schedule (Fig. 3),

$$T(t) = T_{\rm i} - \Gamma t \,, \tag{8}$$

with cooling rate $\Gamma = 0.83\,{\rm K/ns}$. Clearly, this rate is much faster than experimental rates, but slow compared to values typical of simulations [57]. With $\Gamma = 0.83\,{\rm K/ns}$ the total cooling process from 353 K to 3 K takes about 420 ns (4.2×10^8 time steps). As the CPU-time per $\delta t_{\rm outer}$ and united atom is about 4×10^{-7} s (on Intel(R) Xeon(R) Gold 6126 Skylake-based CPU, 2x12 cores), completion of a cooling run for our system of 4640 UAs requires nearly 9 days of computer time. Due to this computational effort we repeat the cooling run only five times for statistical averaging (starting from equilibrated NPT configurations at $T = 353$ K, each separated by 200 ns

from one another) and we only use one of these cooling runs for later equilibration.

For this equilibration the melt configuration at seven working temperatures—213 K, 225 K, 240 K, 253 K, 273 K, 293 K, 353 K—is stored during the cooling run. For the CRC model these temperatures range from the high-T liquid state to the supercooled state near the critical temperature of ideal mode-coupling theory $T_c \approx 215$ K [37] (the experimental glass transition temperature T_g of high-molecular weight 1,4 PBD is $T_g \approx 175$ K [58, 59]). At each working temperature the stored configuration serves as the starting point of an equilibration run that consists of three stages: NPT equilibration, deformation to the equilibrium volume, and NVT equilibration (Fig. 3).

In the NPT equilibration run the system is tempered at $p = 0$ atm over a total duration of 100 ns. This duration suffices to relax the volume, since we find the volume relaxation to last no longer than 30 ns for $T \geq 213$ K. The final 70 ns of the NPT run are then used to determine the equilibrium volume $V(T)$ as the time average over the time series of the volume. In the subsequent deformation stage we start from the instantaneous volume of the final configuration of the NPT run and isotropically change the size of the simulation box until the equilibrium volume $V(T)$ is reached (deform command in LAMMPS [38]). Since the deformation is carried out over a fairly short time of 10 ps, it is necessary to relax residual stresses possibly created by the quenching of the box volume. To this end, the third equilibration stage consists of an NVT run at fixed $V(T)$, during which we monitor the time series of the pressure. For the duration of this third stage we also take 100 ns, which suffices to stabilize the pressure at $p \approx 0$ atm.

Following equilibration we perform NVT production runs at each working temperature. The production run lasts at least 1 μs (10^9 time steps), sometimes even up to 3 μs. With a CPU-time of about 4×10^{-7} s per δt_{outer} and united atom the simulation of 1 μs takes about 20 days of computer time for our system with 4640 UAs. This long time explains why we work with a relatively small system whose linear dimension $L = V^{1/3}$ (≈ 49.3 Å at $T = 353$ K) is not much larger than the average end-to-end distance R_e (≈ 36.5 Å at $T = 353$ K) of the CRC chain. Therefore, finite-size effects cannot be fully excluded, as far as the properties at the scale of a chain are concerned.

To equilibrate the CRC2, CRC4 and FRC models at the seven working temperatures from 213 K $\leq T \leq$ 353 K it is efficient to start from the configuration of the CRC model at the end of the deformation stage at temperature T, fix the corresponding volume $V(T)$, switch U_{tor} according to Eq. (7), and continue the equilibration in the NVT ensemble (at the fixed $V(T)$ from the CRC model). This procedure is justified because we find the pressure to remain at $p = 0$ atm in the NVT runs for the CRC2, CRC4 and FRC models [60]. Following the NVT equilibration we carry out NVT production runs of (at least) 1 μs for data analysis. The final configurations of the production runs are taken as starting points for two further simulations: i) for NPT simulations (of 1 μs) at $p = 0$ atm to calculate the isothermal compressibility from the volume fluctuations [Eq. (17)] for 213 K $\leq T \leq$ 353 K and ii) for cooling runs to determine T_g for the models with reduced or disabled torsions. For the latter runs we take five configurations at $T = 353$ K, separated by 200 ns from each other, that are subsequently subject to a cooling process down to $T = 3$ K at $p = 0$ atm according to Eq. (8). The five cooling runs are used for statistical averaging as for the CRC model. Since the sole difference between the CRC model and the other models is the reduction of U_{tor}, the cooling runs reveal the influence of the torsional potential on the glass transition of PBD.

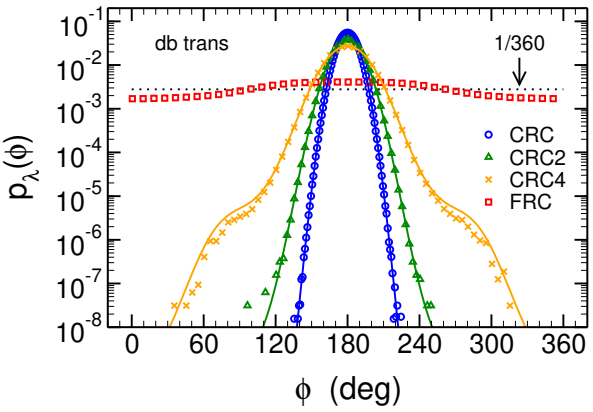

FIG. 4. Log-linear plot of $p_\lambda(\phi)$ versus ϕ for the double bond of the trans conformer at $T = 353$ K. The symbols present the MD results for the CRC (blue circles, $\lambda = 1$), CRC2 (green triangles, $\lambda = 1/2$), CRC4 (orange crosses, $\lambda = 1/4$) and FRC models (red squares, $\lambda = 0$). The full lines show the results from Eq. (9) for the CRC (blue), CRC2 (green) and CRC4 models (orange). The horizontal dotted line indicates the uniform distribution $p_{\lambda=0}(\phi) = 1/360$ expected for the FRC model from Eq. (9).

III. CONFORMATIONAL PROPERTIES

A. Distributions of the torsion angle

A first insight into the influence of reducing the torsional potential may be provided by the distribution of the dihedral angle, $p_\lambda(\phi)$, where λ identifies the different models as defined in Eq. (7). If the dihedral angle was independent of the other potentials, $p_\lambda(\phi)$ would be solely determined by λU_{tor},

$$p_\lambda(\phi) = \frac{\exp(-\lambda U_{\text{tor}}(\phi)/k_B T)}{\int_0^{2\pi} \mathrm{d}\phi \, \exp(-\lambda U_{\text{tor}}(\phi)/k_B T)} \,. \qquad (9)$$

It is therefore instructive to compare Eq. (9) with the distribution obtained from the MD simulations for a given

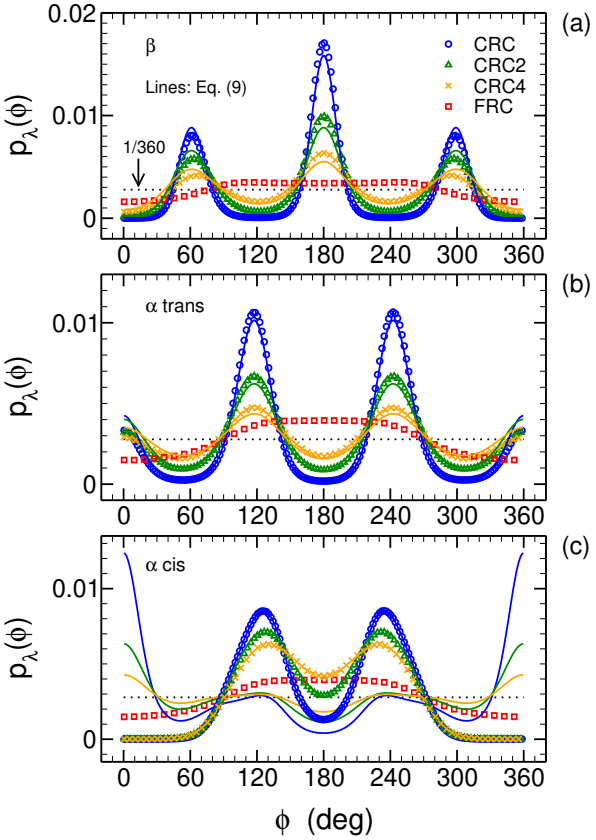

FIG. 5. Plot of $p_\lambda(\phi)$ versus ϕ at $T = 353$ K for three different torsion angles: in panel (a) for the β bond between two monomers, in panel (b) for the α bond adjacent to the double bond of a *trans* monomer (α *trans*), and in panel (c) for the α bond adjacent to the double bond of a *cis* monomer (α *cis*). In all panels, the symbols present the MD results for the CRC (blue circles, $\lambda = 1$), CRC2 (green triangles, $\lambda = 1/2$), CRC4 (orange crosses, $\lambda = 1/4$) and FRC models (red squares, $\lambda = 0$). The full lines show the results from Eq. (9) for the CRC (blue), CRC2 (green) and CRC4 models (orange). The horizontal dotted line indicates the uniform distribution $p_{\lambda=0}(\phi) = 1/360$ expected for the FRC model from Eq. (9).

dihedral. Such a comparison is shown in Fig. 4 for the double bond of the *trans* conformer and in Fig. 5 for the β, α *cis* and α *trans* bonds. As seen from Fig. 4, the distribution from the MD for the CRC model is in excellent agreement with Eq. (9). This is not unexpected because the dihedral associated with the double bond is "hard" conformational variable which is kept close to the equilibrium value by its stiff torsional potential. Reducing this potential could change the situation. However, the agreement between the simulated distribution and Eq. (9) is still good for both the CRC2 and CRC4 models (Fig. 4). While progressive softening of the torsional potential enhances deviations from the *trans* configuration, the population at $\phi = 0°$ or $360°$ vanishes, even for the CRC4 model despite the decrease of the potential barrier of the

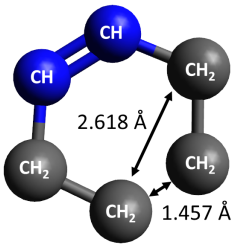

FIG. 6. Sketch of a fragment of a PBD chain comprising a *cis* conformer and 2 adjacent UAs. The bond lengths and bond angles are fixed at their equilibrium values given in Table I and Table II and all dihedral angles (α *cis*, db) are fixed at $\phi = 0°$. This leads to a distance of 1.457 Å between the UAs at the ends of the fragment and to 2.618 Å for the 1-5 (pentane group) distance as indicated. Both distances are substantially smaller than the LJ diameters of the UAs (Table IV), leading to strongly repulsive pair interactions.

cis state by a factor of 4. This implies that *cis*/*trans* isomerization is precluded not only for the CRC model, but also for the CRC2 and CRC4 models. Since the torsional potential for the double bond of the *cis* conformer is only shifted by 180° relative to that of *trans* conformer, the results reported here for the *trans* conformer are found for the *cis* conformer, too (not shown).

The difference between the *cis* and *trans* conformers disappears when the torsional potential is switched off. Then, Eq. (9) predicts a uniform distribution, $p_{\lambda=0}(\phi) = 1/2\pi$. The simulated distribution for the FRC model deviates from this prediction (Fig. 4). The probability of finding ϕ near 180° is increased relative to the uniform distribution, while it is decreased near $\phi = 0°$ or 360°. These deviations stem from intrachain LJ interactions between united atoms separated by four and more bonds, which contribute to the conformational energies and thereby create an effective torsional potential. Such an influence of the LJ potential is expected from the force field parameterization developed in Ref. [24], where intramolecular pair interactions were optimized, in conjunction with the other potentials, so as to reproduce correlations between consecutive torsional states (second-order effects between consecutive pairs of torsions and third-order effects involving three consecutive torsions).

For the FRC model this also implies that similar deviations between the simulated and the uniform distribution must be observed for the other dihedrals of the β, α *cis* and α *trans* bonds. This is illustrated in Fig. 5. As in the case of the double bonds, we see that the probability of adopting torsional angles near 180° is enhanced for the FRC model and suppressed near $\phi = 0°$ or 360°. Deviations between the MD results for the dihedral distributions and the predictions from Eq. (9) are also visible for the CRC, CRC2 and CRC4 models. While Fig. 5(a) and (b) show that the deviations are small for the β and α *trans* bonds, they are large for the α *cis* bond [Fig. 5(c)],

in particular for torsional states near $\phi = 0°$ or 360° which are suppressed in the MD simulation, contrary to the prediction of Eq. (9). Figure 6 explains this result. The sketch shows a *cis* monomer and its two contiguous UAs when all dihedral angles are fixed at $\phi = 0°$. This geometry results in a distance of 2.168 Å between UAs four bonds apart and a distance of 1.457 Å between the outer UAs. Since these united atoms are separated by four or more bonds, they interact by $U_{\rm pair}$, resulting in repulsive energies, $U_{\rm pair}(r = 2.168\ \text{Å}) \approx 66\,\text{kcal/mol}$ and $U_{\rm pair}(r = 1.457\ \text{Å}) \approx 8 \times 10^4\,\text{kcal/mol}$, which are so high that the angle $\phi = 0°$ is never adopted in the simulation. This is an example for the "steric hindrance" (or "pentane") effect known in the literature [23]. Clearly, intrachain correlations beyond those of single torsions are important for the conformational properties of PBD [24].

B. Bond correlations and internal distances

Let $\vec{r}_n$ denote the position of the nth united atom and $\vec{\ell}_n = \vec{r}_{n+1} - \vec{r}_n$ its bond vector. For the UA $m = n + s$ that is separated by s bonds from n, we define the mean-square internal end-to-end distance $R_{\rm e}^2(s)$ and the bond correlation function $P_1(s)$,

$$R_{\rm e}^2(s) = \langle(\vec{r}_{n+s} - \vec{r}_n)^2\rangle\,, \quad P_1(s) = \frac{\langle\vec{\ell}_{n+s}\cdot\vec{\ell}_n\rangle}{l^2}\,, \quad (10)$$

where $l^2 = \langle\vec{\ell}_n^{\,2}\rangle$ is the mean-square bond length. Here $\langle\ldots\rangle$ denotes the thermal average and also the average over all possible pairs (n, m). (Hence, the statistics will deteriorate for $s \to N-1$.) Since $\vec{r}_{n+s} - \vec{r}_n = \sum_{i=n}^{n+s-1}\vec{\ell}_i$, $R_{\rm e}^2(s)$ and $P_1(s)$ are related to each other by

$$R_{\rm e}^2(s) = l^2 s + 2l^2\sum_{k=1}^{s-1}(s-k)P_1(k)\,. \quad (11)$$

Both quantities are of considerable theoretical importance [44, 61, 62] and have often been studied in polymer melt simulations [62–65]. Therefore, we also determine them here.

1. *Parameterization of the MD results and temperature dependence of the characteristic ratio*

As an example for the typical behavior of $P_1(s)$ found for all models in the interval 213 K $\le T \le$ 353 K, Fig. 7 shows the results of the CRC model at $T = 353$ K. If bond correlations were only caused by the bond angle, one would expect from the freely rotating chain model theory an exponential decay $P_1(s) = |\langle\cos\theta\rangle|^s$ [44]. Clearly, this prediction (dashed line in Fig. 7) must underestimate $P_1(s)$ for PBD. It only accounts for correlations between consecutive pairs of bonds $[P_1(s = 1)]$, but not for correlations between more distant pairs along the chain backbone $[P_1(s > 1)]$, resulting from dihedral and interchain

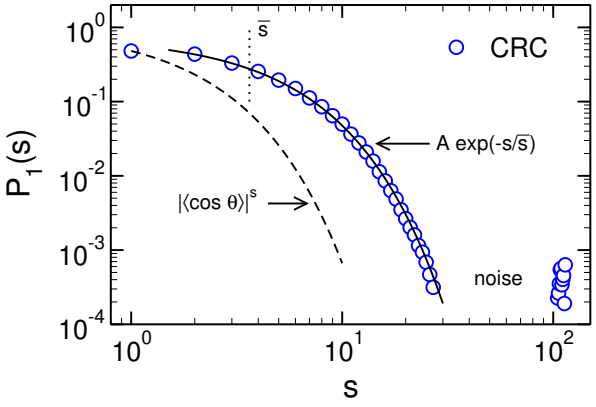

FIG. 7. Log-log plot of $P_1(s)$ versus the number of bonds s $(1 \le s \le N-1)$ for the CRC model (blue circles) at $T = 353$ K. The dashed line indicates the exponential decay based on the freely rotating chain model theory, $|\langle\cos\theta\rangle|^s$ [44]. The solid line represents the fit result to $A\exp(-s/\bar{s})$ with $A = 0.760$ and $\bar{s} = 3.633$ from [42]. $\bar{s}$ is indicated by a vertical dotted line. For $s > 25$ the statistical accuracy of the data deteriorates: $P_1(s)$ can become negative, explaining the gap in the log-log plot for $30 \lesssim s \lesssim 100$. The associated "noise" does not allow an analysis of $P_1(s)$ for $\bar{s} \ll s \le N-1$.

pair interactions. To fit these more distant correlations we use an exponential function $P_1(s) = A\exp(-s/\bar{s})$ with A and $\bar{s}$ as adjustable parameters. This gives a good description of the MD data for $2 \le s \lesssim 25$ (full line in Fig. 7). Figure 7 shows that $P_1(s \approx 25) \sim 10^{-3}$, which is the noise level of our MD results. Since the statistical accuracy does not allow to explore bond correlations for large $s \to N-1$, a viable parameterization of the present data is given by

$$P_1(s) = \begin{cases} \alpha & \text{for } s = 1\,, \\ A\exp(-s/\bar{s}) & \text{for } s > 1\,. \end{cases} \quad (12)$$

where we defined $\alpha = -\langle\cos\theta\rangle$ (> 0). We have analyzed all models for 213 K $\le T \le$ 353 K with Eq. (12). The directly measured values for α and the fit results for A and $\bar{s}$ are compiled in the Supplementary Material.

Insertion of Eq. (12) into Eq. (11) gives

$$R_{\rm e}^2(s) = l^2 s\left[C_\infty - \frac{2}{s}\left(\alpha - A\overline{\alpha} + A\frac{\overline{\alpha} - \overline{\alpha}^{s+1}}{(1-\overline{\alpha})^2}\right)\right]\,, \quad (13)$$

where $\overline{\alpha} = \mathrm{e}^{-1/\bar{s}}$ (< 1) and C_∞ is the characteristic ratio of the infinitely long chain,

$$C_\infty = \lim_{N\to\infty}\frac{R_{\rm e}^2(N-1)}{(N-1)l^2} = 1 + 2(\alpha - A\overline{\alpha}) + \frac{2A\overline{\alpha}}{1-\overline{\alpha}}\,. \quad (14)$$

The characteristic ratio determines the effective bond length $b_{\rm e} = \sqrt{C_\infty}\,l$ [66] and the temperature coefficient κ of the mean-square end-to-end distance $R_{\rm e}^2(N-1)$ of the chain [23],

$$\kappa = 1000\,\frac{\mathrm{d}\ln R_{\rm e}^2(N-1)}{\mathrm{d}T} = 1000\,\frac{\mathrm{d}\ln C_\infty}{\mathrm{d}T}\,. \quad (15)$$

TABLE V. Characteristic ratio C_∞ from Eq. (14) for the various models studied [Eq. (7)] at temperature T. The values are rounded to the first decimal place [42].

	C_∞			
T (K)	CRC	CRC2	CRC4	FRC
213	6.2	6.2	6.0	5.9
225	5.8	6.0	6.0	5.8
240	5.8	5.8	5.9	5.8
253	6.1	5.9	5.8	5.6
273	5.8	5.8	5.8	5.6
293	5.8	5.7	5.7	5.6
353	5.6	5.6	5.6	5.4

The factor of 1000 is introduced in this definition because κ is typically of the order of $10^{-3}\,\mathrm{K}^{-1}$ [24, 67].

Figure 8(a) depicts the ratio $R_e^2(s)/s$ as a function of s for all models at $T = 353$ K. This ratio starts from the mean-square bond length l^2 ($= 2.158\,\text{Å}^2$ [68]), then increases first steeply for small s and eventually levels off when s approaches $N-1$. We find that the dependence $R_e^2(s)/s$ on s can be well fitted by Eq. (13) for all models and temperatures. The dashed line in Fig. 8(a) gives an example for the FRC model. From this analysis we obtain the T dependence of C_∞ (cf. Table V and [42]). The results are plotted as $\ln C_\infty$ versus T in Fig. 8(b). This plot format approximately rectifies the data, yielding negative values for the temperature coefficient in the range $-0.64\,\mathrm{K}^{-1} \lesssim \kappa \lesssim -0.54\,\mathrm{K}^{-1}$ for all models studied. A negative value for κ implies that the chains tend to expand on cooling.

The results for κ may be compared with experimental values [69] and Rotational Isomeric State (RIS) calculations [24, 70]. These studies show that the thermal coefficient is sensitive to the stereochemical composition of PBD. While pure *cis*-PBD has positive κ, negative values are obtained for the pure *trans*-form. For mixed stereoirregular microstructures similar to our simulation model, RIS calculations [70] mostly lead to small negative values of κ ($\sim -0.1\,\mathrm{K}^{-1}$), in resonance with experimental results (where PBD also contains about 9% of vinyl groups in addition to *cis* and *trans* units) [69]. From this comparison we can conclude that our simulation results are in qualitative accord with available literature data ($\kappa < 0$), but the extent of the chain extension on cooling is stronger in the simulation.

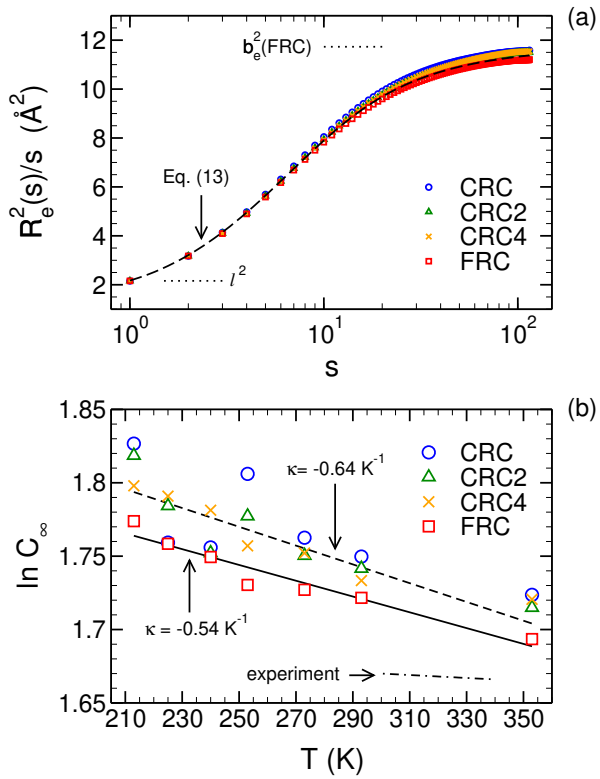

FIG. 8. Panel (a): Plot of the mean-square internal distance $R_e^2(s)$ divided by the number of bonds s versus s ($1 \le s \le N-1$) for the CRC (blue circles), CRC2 (green triangles), CRC4 (orange crosses) and FRC models (red squares). All data refer to $T = 353$ K. The (black) dashed line shows a fit to Eq. (13) for the FRC model. The horizontal dotted lines show respectively the mean-square bond length $l^2 = 2.158\,\text{Å}^2$ and for the FRC model the square effective bond length $b_e^2 = 11.73\,\text{Å}^2$. Panel (b): Temperature dependence of the characteristic ratio C_∞ from Eq. (14) for the CRC (blue circles), CRC2 (green triangles), CRC4 (orange crosses) and FRC models (red squares). The plot format, $\ln C_\infty$ versus T, is motivated by Eq. (15) when assuming κ to be constant. The full line presents a linear fit to the FRC data, yielding $\kappa = -0.54\,\mathrm{K}^{-1}$. The dashed line shows the fit result to the CRC model, leading to $\kappa = -0.64\,\mathrm{K}^{-1}$. The dotted line indicates the experimental result, $\kappa = -0.10\,\mathrm{K}^{-1}$ (obtained for $298\,\mathrm{K} \le T \lesssim 373\,\mathrm{K}$), from Table VIII of Ref. [69].

IV. DENSITY AND COMPRESSIBILITY

A. Continuous cooling through the glass transition: Temperature dependence of the density

A remarkable observation from the previous section is the weak influence of the torsions. Even when switching off all dihedral potentials the conformational properties of the resulting FRC model are very close to those of the CRC model. This finding resonates with the original studies of Refs. [19, 20]. While chain conformations (and liquid structure [4, 19, 20]) remained essentially unperturbed by the torsions, Refs. [19, 20] report a strong influence on dynamic properties: Conformational and structural relaxation in the polymer liquid was found to be enhanced for the FRC model compared to the CRC model at the same T. Based on this observation we expect shifts of T_g to lower temperature when reducing the dihedral potentials.

To test this expectation we use dilatometry, an often employed method in experiments [71–73] and simulations [13, 74–76]. Figure 9 shows the mass density

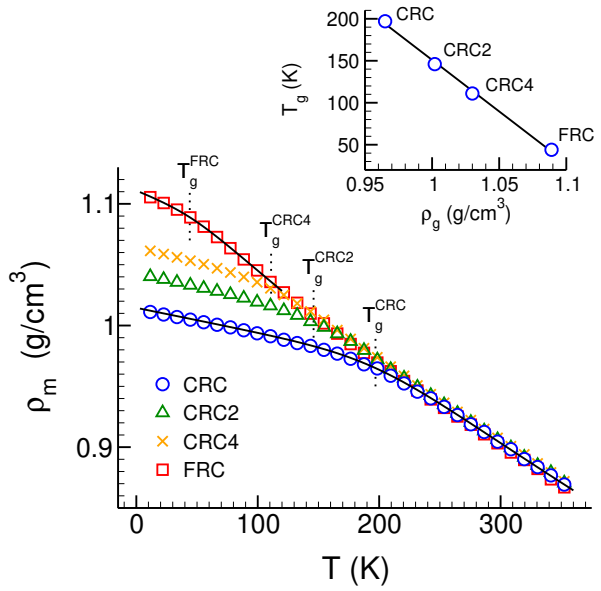

FIG. 9. Mass density $\rho_{\rm m}(T)$ for the CRC (circles), CRC2 (triangles), CRC4 (crosses) and FRC models (squares). All data are obtained from 5 independent cooling runs with rate $\Gamma = 0.83$ K/ns, which were first averaged at each time step and then smoothed by averaging over an interval of $\Delta T = 1$ K. For clarity only every 10th data point is shown. For the CRC and FRC models the (black) full lines exemplify the fits to Eq. (16) with parameters from Table VI. The vertical dotted lines indicate $T_{\rm g}$ from Table VI. Inset: $T_{\rm g}$ versus $\rho_{\rm g}$ from Table VI (symbols). The solid line shows a fit to $T_{\rm g} = A - B\rho_{\rm g}$ yielding $A = 1378\,$K and $B = 1227\,{\rm K}/({\rm g/cm^3})$.

$\rho_{\rm m}(T) = M_0 N_{\rm m} N_{\rm c}/V(T)$ where $V(T) = V(T = T_{\rm i} - \Gamma t)$ is the volume of the system at time t of the cooling process with rate $\Gamma = 0.83$ K/ns [Eq. (8)]. At high temperature, say for $T \gtrsim 250\,$K, we find the same $\rho_{\rm m}(T)$ for all models. The superposition of the data indicates that the influence of the torsions on the density is vanishingly small in the equilibrium liquid. This changes on cooling. For lower T the densities of the different models gradually separate from each other. The CRC model is the first to deviate, falling below the densities of the other models and crossing over to a weaker T dependence than found for the CRC model at high temperature. Similar crossovers occur for the other models but are systematically shifted to lower T with decreasing λ. Since the crossover can be identified with the glass transition, Fig. 9 reveals the coupling of the torsions to the glass transition: $T_{\rm g}$ decreases with the reduction of the dihedral potentials.

For quantitative analysis, we fit the logarithm of $\rho_{\rm m}(T)$ to

$$\ln \rho_{\rm m}(T) = \ln \rho_{\rm g} - (T - T_{\rm g}) \left(\frac{\alpha_{\rm l} + \alpha_{\rm g}}{2} \right) - w \left(\frac{\alpha_{\rm l} - \alpha_{\rm g}}{2} \right) \ln \left[\cosh \left(\frac{T - T_{\rm g}}{w} \right) \right] , \quad (16)$$

TABLE VI. Parameters obtained from fitting Eq. (16) to $\ln \rho_{\rm m}(T)$ [42] for the different models studied : CRC ($\lambda = 1$), CRC2 ($\lambda = 1/2$), CRC2 ($\lambda = 1/4$), FRC ($\lambda = 0$) [cf. Eq. (7)].

λ	w (K)	$\alpha_{\rm l}$ (1/K)	$\alpha_{\rm g}$ (1/K)	$T_{\rm g}$ (K)	$\rho_{\rm g}$ (g/cm^3)
1	57	7.4×10^{-4}	2.0×10^{-4}	197	0.965
0.5	51	7.3×10^{-4}	2.2×10^{-4}	146	1.002
0.25	37	7.2×10^{-4}	2.4×10^{-4}	111	1.030
0	28	8.1×10^{-4}	3.6×10^{-4}	44	1.089

where $\rho_{\rm g} = \rho_{\rm m}(T_{\rm g})$ is the density at $T_{\rm g}$, w the width of temperature interval over which the glass transition occurs, $\alpha_{\rm l}$ the thermal expansion coefficient in the liquid, and $\alpha_{\rm g}$ the expansion coefficient in the glass. Both $\alpha_{\rm l}$ and $\alpha_{\rm g}$ are assumed to be constant. If we further assume that the thermal expansion coefficient $\alpha(T) = -\partial \ln \rho_{\rm m}(T)/\partial T|_p$ can be smoothly interpolated from $\alpha_{\rm g}$ to $\alpha_{\rm l}$ by a hyperbolic tangent, Eq. (16) is obtained upon integration. This method was originally suggested by Dalnoki–Veress *et al.* [77] and applied to the thickness $h(T)$ of polymer films, assuming that the slopes $\partial h/\partial T$ are constant in the melt and glass state of the films. Here we also tested this method, taking the slopes $\partial \rho_{\rm m}/\partial T$, instead of α, as constant in the liquid and in the glass. Details about the fit and a comparison of results obtained from both assumptions—constant slope or constant α—can be found in the Supplementary Material. Since the results closely agree with each other, we focus on Eq. (16) here. As illustrated by the solid lines in Fig. 9 for the CRC and FRC models, we see that Eq. (16) provides a very good parameterization of the density across the glass transition. The quality of the fit is the same for the other models.

For all models studied, Table VI summarizes the fit results to Eq. (16). We find that an excellent description of the shift of $T_{\rm g}$ with λ is given by a power law,

$$T_{\rm g}(\lambda) = T_{\rm g}(0) - [T_{\rm g}(1) - T_{\rm g}(0)]\lambda^{a_T} ,$$

with $a_T = 0.59$. A similar ansatz for the density,

$$\rho_{\rm g}(\lambda) = \rho_{\rm g}(0) - [\rho_{\rm g}(0) - \rho_{\rm g}(1)]\lambda^{a_\rho} ,$$

also provides a very good fit with $a_\rho = 0.53$. Since the exponents a_T and a_ρ are close, we expect an approximately linear correlation between $T_{\rm g}(\lambda)$ and $\rho_{\rm g}(\lambda)$, that is $T_{\rm g}(\lambda) = A - B\rho_{\rm g}(\lambda)$ with positive constants A and B. The inset in Fig. 9 confirms this expectation.

Thus, reduction of the dihedral potentials entails a decrease of $T_{\rm g}$ that is accompanied by an increase of $\rho_{\rm g}$. How can this finding be explained? Following earlier work on PBD [19, 20, 22] and other simulation studies [5, 16–18], we argue that two coupled kinetic arrest mechanisms operate in the PBD melt: (i) intermolecular packing constraints, as in any glass-forming liquid, and (ii) intramolecular torsional barriers, specific to polymers. Relaxational motion of a united atom in PBD requires not only the nearest-neighbor cage to give way

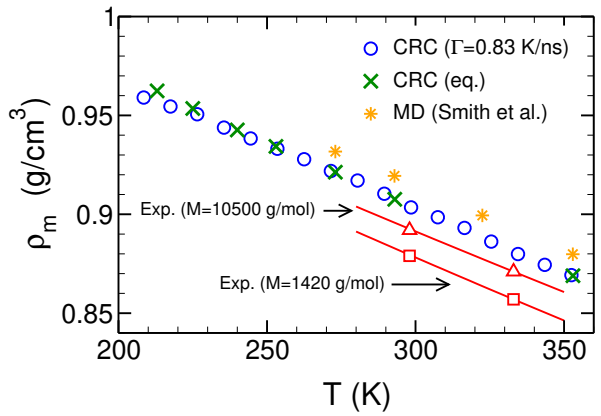

FIG. 10. Comparison of $\rho_{\rm m}(T)$ for the CRC model (molecular weight $M = 1568\,{\rm g/mol}$) with literature results. The circles are taken from Fig. 9, while the crosses show the equilibrium densities for $213\,{\rm K} \le T \le 353\,{\rm K}$. The stars ("Smith et al.") present the (scanned) MD data from Fig. 1 of Ref. [78] for the original 1,4 PBD model at $p = 1$ atm ($M = 1622\,{\rm g/mol}$; PBD with 40% 1,4-*cis*/50% 1,4-*trans*/10% 1,2-vinyl). The circles and triangles show experimental results from Table IV of Ref. [79] for $M = 1420\,{\rm g/mol}$ (circles; PBD with 34% 1,4-*cis*/58% 1,4-*trans*/8% 1,2-vinyl) and $M = 10500\,{\rm g/mol}$ (triangles; PBD with 35% 1,4-*cis*/56% 1,4-*trans*/8% 1,2-vinyl microstructure). The (red) solid lines represent interpolations through the experimental data with $\rho_{\rm m}(T) = \rho_{\rm m}(T = 333)\exp[\alpha(333 - T)]$ and thermal expansion coefficients $\alpha(M = 1420) = 7.4 \times 10^{-4}\,{\rm K}^{-1}$ and $\alpha(M = 10500) = 7.0 \times 10^{-4}\,{\rm K}^{-1}$ from Table IV of Ref. [79].

and thus a release of intermolecular constraints, but also large-angle excursions of the dihedral angles. If, with decreasing T, the dihedrals are progressively bound near the minima of the torsional potential by large barriers, particle mobility is already slowed down by this barrier-induced confinement, requiring less intermolecular constraints for kinetic arrest. Glass formation in the CRC model thus occurs at higher T—and so at lower density—compared to the other models with reduced torsions. In the extreme case of the FRC model, the absence of the dihedral potentials implies that glass formation is mainly driven by intermolecular constraints, akin to flexible or semiflexible bead–spring models without torsional barriers [5, 7, 13]. For such bead–spring models, $T_{\rm g}$ is typically smaller than the LJ temperature unit $\epsilon/k_{\rm B}$, provided ϵ is not too large [7]. This is the case here for PBD. Taking $\epsilon = (\epsilon_{\rm CH_2,CH_2} + \epsilon_{\rm CH,CH})/2$ with the energies of Table IV, one gets $\epsilon/k_{\rm B} \simeq 56\,{\rm K}$ [43], implying that $T_{\rm g} \approx 0.79\,\epsilon/k_{\rm B}$ for the FRC model, in qualitative accord with bead–spring model results [5, 7, 13]. For the CRC model, however, one finds $T_{\rm g} \approx 3.5\epsilon/k_{\rm B}$, which, for bead–spring models, would correspond to the high-T regime of the polymer liquid. This clearly highlights the importance of dihedral barriers as an additional arrest mechanism that, together with collective many-body effects, drives the polymer glass transition.

Finally, Fig. 10 focuses for the CRC model on the T regime of the polymer liquid, where equilibrium can be achieved, and compares $\rho_{\rm m}(T)$ to literature results from simulation [78] and experiment [79]. We see that cooling with $\Gamma = 0.83\,{\rm K/ns}$ can be considered as quasistatic process for $T \gtrsim 250\,{\rm K}$ because the densities from cooling runs (circles) and equilibrium simulations (crosses) agree. For this T regime we also find excellent agreement between the experimental thermal expansion coefficient $\alpha = 7.4 \times 10^{-4}\ {\rm K}^{-1}$ [79] and the simulation results for the present and original (stars [78]) CRC models. On the other hand, the simulated densities are larger than in experiment, suggesting that the CRC model has a lower compressibility. We turn to the compressibility and its variation with the dihedral potential in the following section.

B. Temperature dependence of the compressibility in the polymer liquid

One method to determine the isothermal compressibility κ_T is to monitor the volume fluctuations in NPT simulations

$$\kappa_T = -\frac{1}{V}\left.\frac{\partial V}{\partial p}\right|_T = \frac{\langle V^2\rangle - \langle V\rangle^2}{k_{\rm B}T\langle V\rangle}\ . \qquad (17)$$

This equation is a special case of the theory of the ensemble dependence of thermodynamic fluctuations [80–82].

For temperature range $213\,{\rm K} \le T \le 353\,{\rm K}$ of the equilibrium polymer liquid Fig. 11 depicts the dimensionless compressibility $k_{\rm B}T\rho\kappa_T$ where ρ ($= 4\rho_{\rm m}/M_0$) is the number density of united atoms in the PBD melt. We see that the dihedral potential does not affect the compressibility of the melt; the data for all models studied superimpose, albeit the statistics appears to deteriorate with decreasing T.

Figure 11 plots the compressibility as $1/\sqrt{k_{\rm B}T\rho\kappa_T}$ versus $1/T$. This plot format was suggested by Schweizer and Saltzman based on a prediction from the Polymer-Reference-Interaction-Site-Model theory, yielding [83]

$$\frac{1}{\sqrt{k_{\rm B}T\rho\kappa_T}} = -A + \frac{B}{T}\ , \qquad (18)$$

with $A > 0$ and $B > 0$. Equation (18) was not claimed to be "quantitatively reliable nor rigorous" (cf. Appendix A in [83]), but found to be practically relevant, since it linearizes the experimental data for numerous polymers, including PBD [83]. We scanned the experimental data for PBD from Fig. 4 of Ref. [83] and present them as stars in Fig. 11 together with the fit result to Eq. (18) obtained in [83] (dashed line). Figure 11 shows that the simulation results are in reasonable agreement with experiment and that Eq. (18) describes the numerical data very well in the T range studied. A similar observation has recently been made in a systematic simulation study of the role of cohesive energy and bending rigidity on polymer glass formation using a coarse-grained bead-spring model [7].

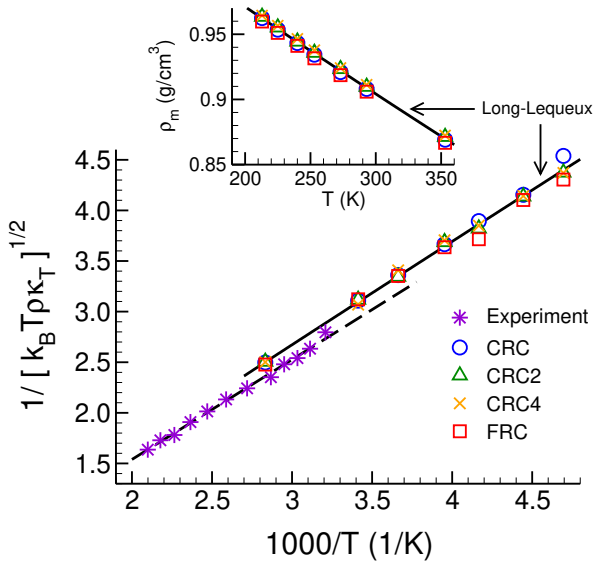

FIG. 11. Temperature dependence of the compressibility for $T \geq 213$ K. The data are rectified as suggested by Eq. (18). The stars are experimental results for PBD scanned from Fig. 4 of Ref. [83]. The dashed line shows Eq. (18) with parameters $A = 0.435$ and $B = 987$ K taken from Table I of Ref. [83]. The other symbols show the simulation results obtained from volume fluctuations [Eq. (17)] for the CRC (circles), CRC2 triangles), CRC4 (crosses) and FRC (squares) models. As the experimental results, they are linearized and can be fitted by Eq. (18) (with $A = 0.384$ and $B = 1019$ K, not shown). The solid line shows the fit to the Long–Lequeux theory from a joint adjustment of the monomer density to Eq. (19) (see inset) and of the compressibility to Eq. (20), yielding $\rho_{m,0} = 1.114\,\mathrm{g/cm^3}$, $\beta = 2.219$, $T_c^{vdW} = 1196\,\mathrm{K}$, $\gamma = 4.754$ [42].

In the past, Schweizer and co-workers derived Eq. (18) from a van–der–Waals (vdW) model for the equation of state, both in the limit of zero pressure approximating atmospheric conditions [84] and in the limit of high pressure [85]. These and further [86] results reveal that Eq. (18) works very well for nonpolar molecular and polymer liquids over a wide range of temperatures and pressures. This is an interesting and potentially significant finding. Equation (18) is then employed as a key input in a mapping of a hard-sphere fluid to molecular liquids [84] and polymer melts [9, 10]. This mapping is used in the elastically collective nonlinear Langevin equation (ECNLE) theory [9, 10, 84] and its extensions to polymer films [87–89] to convert the density dependence of the dynamics in hard-sphere fluids to the T dependence of the dynamics in thermal fluids.

Given the proposed universal relationship between κ_T and T, the recent simulation study by Xu *et al.* [7] also examined the validity of Eq. (18) for a flexible and semiflexible bead-spring model and a broad range of cohesive interaction strengths (i.e. depths of the LJ potential). It is found that Eq. (18) can linearize the simulation data at low T (typically below the onset temperature of super-Arrhenius increase of the α relaxation time), while deviations occur at high T. The authors conclude that further analysis is desirable [7]. If Eq. (18) was established, it could not only serve as input for the ECNLE theory but would also allow to determine the cohesive energy parameter of the Generalized Entropy Theory [8], a further developing theory for polymer glass formation.

In this respect, it is interesting that a vdW approach akin to that of Schweizer and coworkers was proposed before by Long and Lequeux [90]. The Long–Lequeux model is closely related to the cell model of the liquid state [91] and was also extended to account for effects of pressure and temperature in polymer blends [92]. To model the pressure-volume-temperature behavior of polymer melts Long and Lequeux start from a vdW-like ansatz for the free energy. Minimization of the free energy with respect to density implies zero pressure conditions and leads to the following expressions for the equilibrium density,

$$\rho = \frac{\rho_0}{2}\,\frac{1+\sqrt{1-T/T_c^{vdW}}}{1+\beta\left(1-\sqrt{1-T/T_c^{vdW}}\right)/2}\,, \qquad (19)$$

and compressibility,

$$\frac{1}{\kappa_T} = \frac{k_B T \rho_0}{2\gamma^2}\left[1+\sqrt{1-\frac{T}{T_c^{vdW}}}\right]^3 \times \left[\frac{1}{\left(1-\sqrt{1-T/T_c^{vdW}}\right)^2} - \frac{T_c^{vdW}}{T}\right]. \qquad (20)$$

Here ρ_0 is the maximum close-packing density and T_c^{vdW} the temperature at which air would become a good solvent for the polymer. Clearly, this hypothetical temperature must be very high so that $T_g \lesssim T \ll T_c^{vdW}$ is the temperature regime where the theory is expected to hold [90]. The two other parameters, β and γ, are numbers that account for incompressibility, that is, for the constraint that the local density in the system needs to be smaller than ρ_0.

A similar incompressibility constraint is not implemented by Schweizer and coworkers, implying that $\beta = 0$ and $\gamma = 1$ [90]. Indeed, Eq. (19) for $\beta = 0$ gives back Eq. (6) from Ref. [84]. In this study [84], Mirigian and Schweizer obtain Eq. (18) for zero pressure in the limit $T \ll T_c^{vdW}$. Since zero pressure corresponds to the minimization condition of the free energy [90], we carry out a low-T expansion of Eqs. (19) and (20). This gives back Eq. (18) with $A = (5-\beta)/2\gamma$ and $B = 4T_c^{vdW}/\gamma$. Inserting the values for $(\beta, \gamma, T_c^{vdW})$ from Fig. 11 we get $A = 0.292$ and $B = 1006\,\mathrm{K}$ [42] . These predictions are slightly different from the best fit to Eq. (18) (cf. Fig. 11), which is not unexpected due to the low-T approximation employed. Since Eqs. (19) and (20) avoid the low-T approximation, they should apply over a larger temperature range. Indeed, Ref. [90] suggests that Eqs. (19) and (20)

provide a consistent description of both ρ and κ_T for supercooled polymer melts down to T_g. Therefore, we fitted Eqs. (19) and (20) to our simulation results for the all models studied [42]. As shown in Fig. 11, we find good agreement for ρ (solid line in the inset) and κ_T (solid line in the main figure), with values for the fit parameters that are in reasonable accord with the results reported in Ref. [90] for other hydrocarbon polymers, such as polystyrene or poly(isobutylene).

Due to the encouraging nature of this comparison between our simulations and the Long–Lequeux model, we will utilize Eqs. (19) and (20) in the modeling of the specific heat at constant pressure in the next section.

V. INTERNAL ENERGY AND HEAT CAPACITY

Let $\boldsymbol{x}$ denote the microstate of the PBD melt containing N_c polymers with N united atoms each. The hamiltonian is written as

$$\mathcal{H}(\boldsymbol{x}) = K(\boldsymbol{x}) + U_{\rm tot}(\boldsymbol{x}) \; , \tag{21}$$

where K is the total kinetic energy and $U_{\rm tot}$ is the total potential energy consisting of valence terms (bond, bond angle, dihedral) and pair (Lennard–Jones) interactions. As explained in Sec. II C, the simulations are carried out in two steps: First, NPT relaxation to get the average volume $V = V(T, p, N_cN)$ corresponding to temperature T and pressure p (= 0). Second, NVT production runs by imposing the volume $V(T, p, N_cN)$. During the canonical production runs the internal energy U is determined by $U = \langle \mathcal{H}(\boldsymbol{x}) \rangle$. Since $V = V(T, p, N_cN)$, we get the internal energy at constant pressure, $U(T, p, N_cN)$, from these production runs.

In Sec. V A we first discuss the contributions from the different terms of $U_{\rm tot}$ to the internal energy before we turn to the heat capacity in Sec. V B.

A. Temperature dependence of the internal energy

1. *Bond length and bond angle potentials*

The bond length ℓ is subjected to the harmonic bond potential of Eq. (1). Since the force constant $K_{\rm bond}$ is large, ℓ is constrained to remain close to the equilibrium bond length ℓ_0. It is therefore reasonable to assume that the fluctuations of ℓ are determined solely by Eq. (1), i.e. that the bond lengths are independent of each other and of the potentials for the bond angles, torsion angles and pair interactions. As a polymer chain has $N - 1$ bonds, the average extensive bond length energy ($E_{\rm bond}$) is given by [42]

$$E_{\rm bond}(T, p, N_cN) \simeq N_cN \left(1 - \frac{1}{N}\right) \frac{1}{2}\, k_BT \; . \tag{22}$$

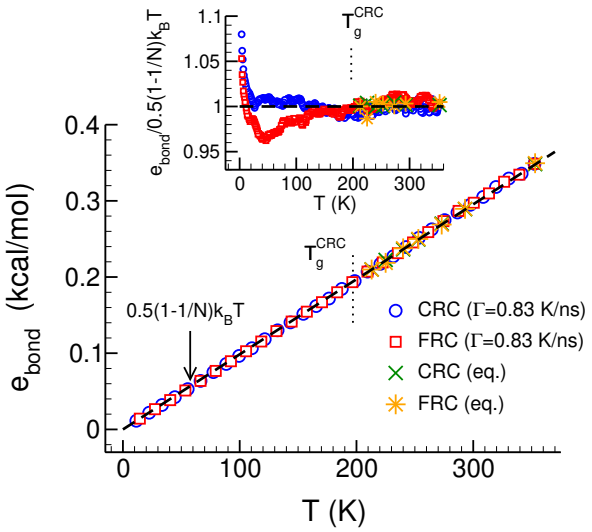

FIG. 12. Intensive bond length energy $e_{\rm bond}$ (= $E_{\rm bond}/N_cN$) versus T for the CRC and FRC models. Results from continuous cooling runs with rate Γ = 0.83 K/ns (CRC: circles, FRC: squares) are compared to equilibrium data for 213 K ≤ T ≤ 353 K (CRC: crosses, FRC: stars). The black dashed line depicts Eq. (22). The vertical dotted line indicates T_g = 197 K of the CRC model (cf. Table VI). Inset: Plot of the ratio $e_{\rm bond}/[(1 - 1/N)k_BT/2]$ versus T using the same data as in the main panel.

Figure 12 compares Eq. (22) with simulation data for the intensive energy $e_{\rm bond}$ (= $E_{\rm bond}/N_cN$) of the CRC and FRC models. Two data sets are shown from cooling runs with rate $\Gamma = 0.83$ K/ns and equilibrium results for $T \geq 213$ K. We see that both data sets agree well for $T \geq 213$ K. Moreover, the main panel of Fig. 12 suggests that Eq. (22) gives an excellent description of the T dependence, not only for the equilibrated polymer liquid, but also for the glass down to lowest T studied. The inset provides a more critical test. If Eq. (22) was valid for all T, the ratio $e_{\rm bond}/[(1 - 1/N)k_BT/2]$ should fluctuate around 1. While this is the case for $T \gtrsim 140$ K, the ratio systematically increases as $T \to 0$. However, the deviations are weak. To a good approximation, the assumption of independent bond lengths is therefore justified and the rate $\Gamma = 0.83$ K/ns is sufficiently slow so that the cooling process can be considered as quasistatic for ℓ.

Since the bond angle is also subjected to a harmonic potential with a large $K_{\rm bend}$ [Eqs. (2), (3)], an approach analogous to that of ℓ can be used to estimate the average extensive bond angle energy ($E_{\rm ang}$). As there are $N - 2$ angles per chain, $E_{\rm ang}$ is given by [42]

$$E_{\rm ang}(T, p, N_cN) \simeq N_cN \left(1 - \frac{2}{N}\right) \frac{1}{2}\, k_BT \; . \tag{23}$$

Figure 13 compares Eq. (23) with the simulation results for the CRC and FRC models. The intensive energies $e_{\rm ang}$ (= $E_{\rm ang}/N_cN$) from cooling runs and equilibrium

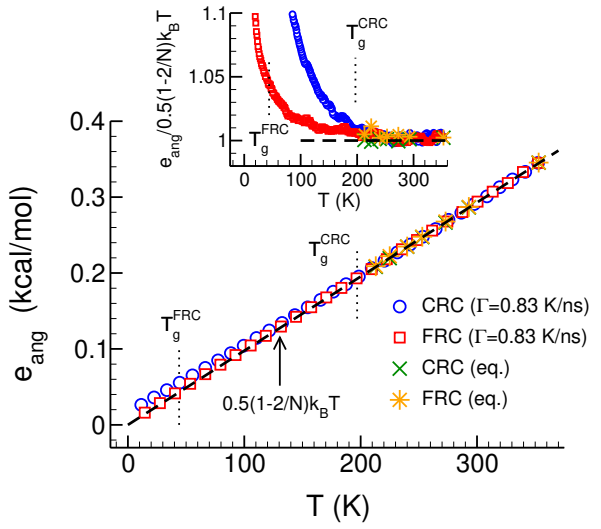

FIG. 13. Intensive bond angle energy $e_{\rm ang}$ ($= E_{\rm ang}/N_{\rm c}N$) versus T for the CRC and FRC models. Results from continuous cooling runs with rate $\Gamma = 0.83$ K/ns (CRC: circles, FRC: squares) are compared to equilibrium data for $213\,{\rm K} \le T \le 353\,{\rm K}$ (CRC: crosses, FRC: stars). The black dashed line depicts Eq. (23). The vertical dotted lines indicate $T_{\rm g} = 197\,{\rm K}$ and $T_{\rm g} = 44\,{\rm K}$ of the CRC model and FRC model, respectively (cf. Table VI). Inset: Plot of the ratio $e_{\rm ang}/[(1-2/N)k_{\rm B}T/2]$ versus T using the same data as in the main panel. For $T \to 0$ the ratio increases to about 1.6 for the FRC model and to about 5.6 for the CRC model.

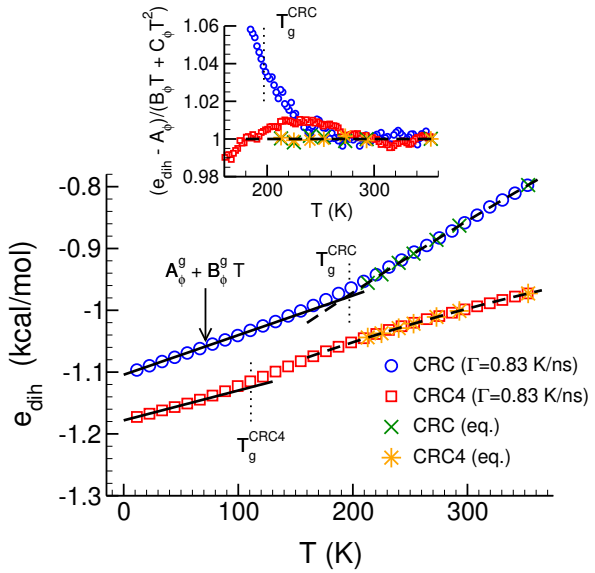

FIG. 14. Intensive energy of the dihedral angles $e_{\rm dih}$ ($= E_{\rm dih}/N_{\rm c}N$) versus T for the CRC and CRC4 models. For the CRC4 model $e_{\rm dih}$ is shifted downward by -0.95 kcal/mol to put the energies on the same scale as $e_{\rm dih}$ of the CRC model. Results from continuous cooling runs with rate $\Gamma = 0.83$ K/ns (CRC: circles, CRC4: squares) are compared to equilibrium data for $213\,{\rm K} \le T \le 353\,{\rm K}$ (CRC: crosses, CRC4: stars). The black dashed lines depict a fit to the equilibrium data with Eq. (24). In the glassy phase the black solid lines show the fit result to $e_{\rm dih}(T) = A_\phi^{\rm g} + B_\phi^{\rm g} T$ [42]. The vertical dotted lines indicate $T_{\rm g} = 197\,{\rm K}$ for the CRC model and $T_{\rm g} = 111\,{\rm K}$ for the CRC4 model (cf. Table VI). Inset: Plot of $(e_{\rm dih} - A_\phi)/(B_\phi T + C_\phi T^2)$ versus T to examine the quality of the fit with Eq. (24).

simulations agree with each other for $T \ge 213$ K and also with Eq. (23). However, for $T \to 0$ systematic deviations from Eq. (23) appear. These deviations become pronounced in the glass transition zone around $T_{\rm g}$, as illustrated in the inset of Fig. 13. Clearly, the softer force constant $K_{\rm bend}$, compared to $K_{\rm bond}$, enables larger fluctuations of the bond angles and so their stronger coupling to the vitrifying melt.

2. *Dihedral potential*

The results from Sec. III A show that a harmonic expansion around the minima of the dihedral potentials cannot be sufficient to describe the T dependence of the average torsion energy $E_{\rm dih}(T, p, N_{\rm c}N)$ in the polymer liquid. Anharmonic effects need to be taken into account. A possible scheme to include anharmonicity is to expand $E_{\rm dih}(T, p, N_{\rm c}N)$ in powers of T:

$$E_{\rm dih}(T, p, N_{\rm c}N) = N_{\rm c}N\Big[A_\phi(p) + B_\phi(p)T + C_\phi(p)T^2 + \mathcal{O}(T^3)\Big]\,, \quad (24)$$

where the coefficients $A_\phi(p)$, $B_\phi(p)$, $C_\phi(p)$, etc. are (p dependent) fit parameters. This ansatz is inspired by similar approaches used in the potential energy landscape description of supercooled liquids and glasses (cf. Sect. 6.2 of [93]).

Figure 14 shows that already the first anharmonic correction (C_ϕ) suffices to give an excellent fit to the simulation data for $T \ge 213$ K for the CRC and CRC4 models. (Results for the CRC2 model, not shown, are the same; the FRC model has no torsional potential.) For the CRC model $|C_\phi T|$ is by a factor of about 10 smaller than B_ϕ, while this factor is about 5 for the CRC4 model [42]. For the CRC4 model anharmonic corrections are larger, as expected. Still, for both models these corrections are relatively small, justifying the truncation of Eq. (24) at second order. However, the relatively small anharmonicity does not imply a weak coupling of the torsions to the vitrifying matrix. On the contrary, the impact of the glass transition is clearly visible in the main panel of Fig. 14. For both models the cooling process is too fast for the melt to stay at equilibrium on approach to $T_{\rm g}$. Accordingly, the dihedral energy at low T bends over to a weaker temperature dependence. For $T \to 0$ a harmonic approximation, $e_{\rm dih}(T) = A_\phi^{\rm g} + B_\phi^{\rm g} T$, provides a good description (solid lines in Fig. 14). The fit results for the ground state energy $A_\phi^{\rm g}$ [42] are found to be much larger than the values expected from the torsional potentials,

which are given by the energy minimum at 180° of the β dihedral (-5.28281 kcal/mol for the CRC model and -1.32070 kcal/mol for the CRC4 model). This exemplifies the nonequilibrium character of the glass created by the cooling process.

3. *Pair interactions*

From the viewpoint of the pair interactions the PBD model corresponds to a binary LJ mixture [42]. For LJ and other simple liquids various approaches to decribe the T dependence of the excess energy have been proposed, see e.g. [94, 95]. One influential theory was developed by Rosenfeld and Tarazona (RT) [94]. The RT theory starts from an accurate approximation for the excess free energy functional of densely packed hard spheres and uses thermodynamic perturbation theory to extend the theory to continuous ("soft") potentials. First-order perturbation theory around $\eta = 1$ packing fraction gives for the excess internal energy ($E^{\rm ex}$) of a three-dimensional classical bulk fluid with N particles the following constant volume (particle density ρ) and constant temperature expression (cf. Eq. (34) in Ref. [94]):

$$\frac{E^{\rm ex}(\rho,T)}{N} = A_{\rm RT}(\rho) + B_{\rm RT}(\rho)T^{3/5} + \cdots \ .$$

The leading $T^{3/5}$ term is expected to be accurate for large densities (near freezing) and predominantly repulsive interactions [94]. It implies that the excess isochoric heat capacity ($C_V^{\rm ex} = \partial E^{\rm ex}/\partial T|_{V,N}$) increases with decreasing temperature as $C_V^{\rm ex} \propto T^{-2/5}$.

A detailed simulation study of the T dependence of $C_V^{\rm ex}$ was carried out in Ref. [96] for 18 model liquids with different stoichiometric composition, molecular topology and interactions. It was found that the RT expression $C_V^{\rm ex} \propto T^{-2/5}$ provides a better approximation for liquids with strong correlations between equilibrium fluctuations of virial and potential energy, i.e., for so-called "Roskilde-simple" liquids [97]. For instance, the Kob–Andersen binary LJ mixture [49–52] is a Roskilde-simple liquid (for $\rho \simeq 1.2$ in LJ units) obeying $C_V^{\rm ex} \propto T^{-2/5}$ [52, 96]. Due to the results reported in Ref. [96] it is tempting to test whether the ansatz,

$$E_{\rm pair}(T,p,N_{\rm c}N) \simeq N_{\rm c}N\Big[A_{\rm RT}(p) + B_{\rm RT}(p)T^{3/5}\Big] \ , \quad (25)$$

can provide a good description for the pair interactions of the PBD model.

Figure 15 shows that the description is indeed excellent. The fit to Eq. (25) was carried out for the equilibrated polymer liquid in the interval $213\,{\rm K} \le T \le 353\,{\rm K}$ (dashed line), where the pair energies of the CRC and FRC models (nearly) coincide. Interestingly, the extrapolation of the fit to low T agrees with the FRC results from the cooling run down to the temperature regime where the glass transition of the FRC model occurs (see also the inset in Fig. 15 supporting the quality of the fit).

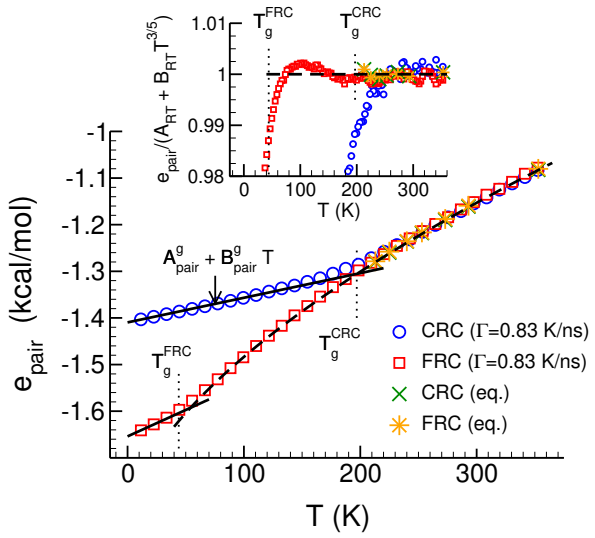

FIG. 15. Intensive LJ energy $e_{\rm pair}$ ($= E_{\rm pair}/N_{\rm c}N$) versus T for the CRC and FRC models. Results from continuous cooling runs with rate $\Gamma = 0.83$ K/ns (CRC: circles, FRC: squares) are compared to equilibrium data for $213\,{\rm K} \le T \le 353\,{\rm K}$ (CRC: crosses, FRC: stars). The dashed line depicts Eq. (25) with $A_{\rm RT} = -1.83785$ kcal/mol and $B_{\rm RT} = 2.23478\times10^2$ kcal/mol K$^{3/5}$. These parameters are the average values for $A_{\rm RT}$ and $B_{\rm RT}$ obtained from fits to the equilibrium data of all models in the interval $213\,{\rm K} \le T \le 353\,{\rm K}$ [42]. In the glassy phase the solid line indicate the fit result to $e_{\rm pair}(T) = A^{\rm g}_{\rm pair} + B^{\rm g}_{\rm pair}T$ [42]. The vertical dotted lines indicate $T_{\rm g} = 197\,{\rm K}$ for the CRC model and $T_{\rm g} = 44\,{\rm K}$ for the FRC model from Table VI. Inset: Plot of the ratio $E_{\rm ang}$ divided by Eq. (25) versus T to examine the quality of the fit by Eq. (25) in the liquid phase.

The impact of the glass transition is clearly visible in the main panel of Fig. 15. For the both models we find, as for the dihedral angles, that the cooling process is too fast for the melt to stay at equilibrium when the temperature crosses the respective $T_{\rm g}$. Accordingly, the pair energy at low T is larger than the extrapolated liquid curve. For $T \to 0$ a harmonic approximation provides again an excellent description of the energy (solid lines in Fig. 15), as expected for a classical solid.

B. Heat capacity of the polymer liquid

The thermodynamic relation between the (extensive) heat capacity at constant pressure C_p and at constant volume C_V is given by

$$C_p = C_V + TV\frac{\alpha^2}{\kappa_T} = C_V + N_{\rm c}N\frac{T\alpha^2}{\rho\kappa_T} \ , \quad (26)$$

where α is the thermal expansion coefficient, κ_T the isothermal compressibility and ρ the number density of united atoms in the system. If we consider the heat capacity as the ability of a material to take up energy and to

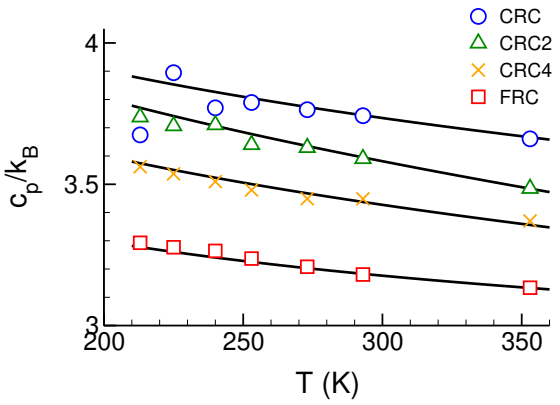

FIG. 16. Specific heat at constant pressure c_p versus T from the equilibrium polymer liquid ($213\,\mathrm{K} \le T \le 353\,\mathrm{K}$) of the CRC, CRC2, CRC4 and FRC models. The symbols present the results from enthalpy fluctuations for c_p. The solid lines indicate c_p obtained from the temperature derivative of the enthalpy, i.e. by inserting Eqs. (29), (30), (31) into Eq. (27).

statistically distribute this energy over all degrees of freedom, it is natural to report the specific heat ($c = C/N_\mathrm{c}N$) divided by k_B because this quantity can be interpreted as the number of degrees of freedom per particle contributing to the heat capacity at temperature T.

Figure 16 shows such a plot for the phase of the equilibrium polymer liquid of all models studied. The specific heat at constant pressure c_p was obtained from the fluctuations of the enthalpy $H = U + pV$ in the NPT runs (symbols) [98]. Alternatively, c_p can also be calculated by

$$c_p = \frac{1}{N_\mathrm{c}N}\left.\frac{\partial H}{\partial T}\right|_{p,N_\mathrm{c}N} = \frac{1}{N_\mathrm{c}N}\left.\frac{\partial U}{\partial T}\right|_{p,N_\mathrm{c}N} , \qquad (27)$$

where $U(T, p, N_\mathrm{c}N)$ is the internal energy. The pV term of H does not contribute because the NPT simulations are performed at $p = 0$. The internal energy is given by

$$U = E_\mathrm{kin} + E_\mathrm{bond} + E_\mathrm{ang} + E_\mathrm{dih} + E_\mathrm{pair} \qquad (28)$$

with E_kin being the average extensive kinetic energy [99],

$$E_\mathrm{kin} = \langle K \rangle = \frac{3}{2}\, N_\mathrm{c}N k_\mathrm{B} T \, .$$

The kinetic energy and the energies for the bond length [Eq. (22)] and bond angle [Eq. (23)] give the following contribution to the specific heat ($N = 116$)

$$\frac{1}{N_\mathrm{c}N}\left.\frac{\partial}{\partial T}(E_\mathrm{kin} + E_\mathrm{bond} + E_\mathrm{ang})\right|_{p,N_\mathrm{c}N} = \left[\frac{5}{2}\left(1 - \frac{3}{5N}\right)\right] k_\mathrm{B} = 2.487\, k_\mathrm{B} \, . \qquad (29)$$

For the dihedral and pair potentials we find from Eq. (24) and Eq. (25)

$$\frac{1}{N_\mathrm{c}N}\left.\frac{\partial E_\mathrm{dih}}{\partial T}\right|_{p,N_\mathrm{c}N} = B_\phi - 2|C_\phi|T \, , \qquad (30)$$

$$\frac{1}{N_\mathrm{c}N}\left.\frac{\partial E_\mathrm{pair}}{\partial T}\right|_{p,N_\mathrm{c}N} = \frac{3}{5}\, B_\mathrm{RT}\, T^{-2/5} \, . \qquad (31)$$

By adding Eqs. (29), (30) and (31) the solid lines in Fig. 17 are obtained, which agree with the results from the enthalpy fluctuations for all models (barring perhaps the data point at $T = 213$ K for the CRC model, which is the least precise due to the much longer relaxation time of the CRC model compared to the other models at low T). Of course, this agreement is expected for systems at thermal equilibrium. Here it illustrates, on the one hand, the internal consistency of the simulation, i.e., of the thermostating/barostating methods and the length of the equilibration and production runs. On the other hand, the splitting of the U into its contributions according to Eq. (28) allows to obtain further insight into the T dependence of c_p. For instance, since $E_\mathrm{dih} = 0$ for the FRC model, only E_pair determines the T dependence of c_p via Eq. (31). As the coefficient B_RT is (nearly) the same for all models studied [42], the difference between the FRC model and the other models thus singles out the contribution of the dihedral energy to c_p.

For the CRC model Fig. 17 further details this discussion. With the value for B_ϕ from [42] the first term of Eq. (30) adds a constant of about $0.701 k_\mathrm{B}$ to c_p. Together with Eq. (29) this implies an overall constant contribution of about $3.138 k_\mathrm{B}$ to the specific heat, resulting from the kinetic energy and harmonic intrachain contributions (bond length, bond angle, and B_ϕ). This baseline accounts for the major part of the specific heat (dotted line in Fig. 17), while the T dependent parts from Eq. (30) and Eq. (31) represent less than one k_B. The T dependence is dominated by the pair interactions, as seen from dash-dotted line in Fig. 17.

The specific heat at constant volume can be calculated from the fluctuations of the hamiltonian $\mathcal{H}$ in the NVT simulations

$$c_V = \frac{1}{N_\mathrm{c}N}\,\frac{1}{k_\mathrm{B}T^2}\left[\langle \mathcal{H}^2 \rangle - \langle \mathcal{H} \rangle^2\right] . \qquad (32)$$

The squares in Fig. 17 show the result of this calculation. As expected, $c_V < c_p$. Alternatively, c_V can be obtained from c_p via Eq. (26),

$$c_V = \frac{1}{N_\mathrm{c}N}\left.\frac{\partial H}{\partial T}\right|_{p,N_\mathrm{c}N} - \frac{T\alpha^2}{\rho\kappa_T} \, . \qquad (33)$$

The first term is known from Eq. (27), the second term can be obtained from the Long–Lequeux model [Eqs. (19), (20)]. Then, the right-hand side of Eq. (33) can be calculated. The dashed line in Fig. 17 shows that the result of this calculation agrees with Eq. (32), as it should be for thermally equilibrated systems. Here this

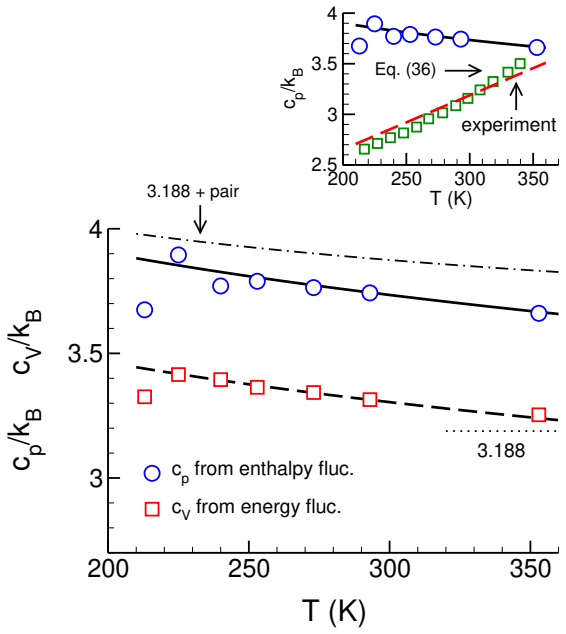

FIG. 17. Specific heat at constant pressure c_p and constant volume c_V versus T from equilibrium simulations of the CRC model. The symbols present the results from enthalpy fluctuations for c_p (circles) and energy fluctuations for c_V (squares). The solid line indicates c_p obtained by inserting Eqs. (29), (30), (31) into Eq. (27). The dashed line shows c_V calculated from Eq. (33) as discussed in the text. The horizontal dotted line indicates the sum of Eq. (29) and B_ϕ ($= 0.701\,k_B$ [42]) from Eq. (30), yielding the constant $3.188\,k_B$. When adding the pair energy [Eq. (31)] to this constant one gets the dash-dotted line. The difference between the circles and the dash-dotted line corresponds to the contribution of the T dependent part of the dihedrals [i.e. $-2|C_\phi|T$ from Eq. (30)]. Inset: Comparison to experiment. The circles and solid line are the results for c_p from the main panel. The dashed line shows the experimental data from Ref. [100], i.e. Eq. (34) divided by $4R$ with R being the gas constant. The (green) squares depict the results from Eq. (36) using the experimental data for the solid state from Fig. 9 of [100] as a proxy to account for contributions from quantum mechanical vibrations in the experimental system.

agreement illustrates again the internal consistency of the MD simulations, i.e. of the choices made for the simulation parameters (barostat, thermostat, switching procedure from the NPT to NVT ensemble, etc.).

C. Heat capacity of the polymer liquid: Comparison with experiment

The inset of Fig. 17 compares the simulation results for c_p (circles with solid line) with the experimental heat capacity of liquid 1,4 PBD (dashed line) [100]. The experimental data refer to *cis*-PBD and *trans*-PBD. Both polymers crystallize, but have identical c_p in the liquid phase. To parameterize the T dependence of liquid PBD Ref. [100] recommends the following equation for the specific heat per monomer:

$$c_p = 52.63 + 0.178\,T \;\; (\mathrm{J/(mol\,K)})\,. \tag{34}$$

Since PBD has 4 united atoms per monomers, the dashed line in the inset shows Eq. (34) divided by $4\,R$ with R being the gas constant. We see that the order of magnitude is the same for both simulation and experiment, but the T dependence is different: The simulated c_p increases upon cooling, whereas the experimental c_p decreases.

How can this difference be explained? A comprehensive discussion of the thermal analysis of polymers is provided in the book by Wunderlich [101]. Section 2.3.9 of [101] reports that the heat capacity of many liquid polymers increases linearly with temperature. Equation (34) thus represents a typical behavior found in experiment. The linear T dependence is interpreted as resulting from the superposition of three contributions [102]:

$$C_p = C_{\mathrm{vib}}(T) + C_{\mathrm{conf}}(T) + \frac{TV\alpha^2}{\kappa_T}\,, \tag{35}$$

where C_{vib} denotes the vibrational heat capacity at constant volume and C_{conf} the (nonvibrational) configurational contribution to C_p due to backbone rotations and intermolecular interactions. Analysis for several hydrocarbon polymers in [102] shows that, even in the liquid, the major contribution to C_p comes from C_{vib}. As explained in [100–102], C_{vib} can be calculated from the vibrational spectrum of a polymer by considering two modes of vibration: "skeletal modes", involving torsion vibrations, bond-angle vibrations as well as collective vibrations along the chain backbone, and "group modes", involving vibrations of small groups of atoms, e.g. stretching vibrations of the CC and CH bonds, bending vibrations of the angle in CH_2, etc. (see Fig. 2.48 on p. 123 in [101] and Table 4 in [100]). To calculate $C_{\mathrm{vib}}(T)$ both modes are treated quantum mechanically, based on the Debye and Einstein theories for the heat capacity. The Debye and Einstein theories predict the heat capacity to increase toward the classical limit with increasing T. Applications reveal that this classical limit is not yet reached in the experimentally studied T regime of the polymer liquid (cf. [102] and p. 138 in [101]). Therefore, $C_{\mathrm{vib}}(T)$ still increases with T. Although $C_{\mathrm{conf}}(T)$ and $TV\alpha^2/\rho\kappa_T$ are found to decrease upon heating, this decrease is weaker than the increase of $C_{\mathrm{vib}}(T)$. Therefore, the sum of the three contributions still leads to an increase of C_p with T, which can be fitted by a linear T dependence.

Clearly, our classical united-atom model must fail to reproduce this behavior: Hydrogen atoms are not explicitly taken into account and quantum mechanical effects are absent. In our case, c_{vib} is a constant given by the classical result as a multiple of k_B.

If quantum mechanical skeletal and group vibrations are really the cause of the discrepancy between the simulated and experimental c_p, can we approximately correct

for these missing effects? As an attempt to do so, we scanned the calculated heat capacity $C_p^{\rm solid}$ for the solid state from Fig. 9 of Ref. [100],

$$C_p^{\rm solid}(T) = C_{\rm vib}(T) + \frac{TV\alpha^2}{\kappa_T} \ ,$$

and used this as a proxy to account for quantum mechanical vibrational contributions. The resulting prediction for the experimental specific heat then reads

$$c_p \approx c_p^{\rm solid}(T) + \left[\frac{3}{5}\,\frac{B_{\rm RT}}{T^{2/5}} - 2|C_\phi|T\right] \ , \qquad (36)$$

where the term in angular brackets stems from Eqs. (30) and (31). This term replaces $C_{\rm conf}$ in Eq. (35) because it accounts for contributions to c_p due to anharmonic dihedral energies and soft pair interactions in the polymer liquid.

The inset in Fig. 17 shows that Eq. (36) is reasonable. Using $c_p^{\rm solid}(T)$ from experiment inverts the T dependence originally found from the simulation, now yielding semiquantitative agreement with the experimental data (squares in the inset). Moreover, this agreement also implies that the term $[3B_{\rm RT}/5T^{2/5} - 2|C_\phi|T]$ in Eq. (36) provides a good description of the configurational contribution to c_p compared to experiment.

The conclusions made here about quantum effects are also supported by a recent study [103] comparing simulated heat capacities for 11 hydrocarbon oligomers and commodity polymers in the liquid phase with experimental data. This study demonstrates the importance of harmonic quantum corrections to get good agreement with experiment and also suggests computational methods to implement these corrections in classical molecular simulations, as an alternative to a full quantum mechanical treatment of all atoms in the polymer [104] (see also references in [103]).

VI. SUMMARY AND DISCUSSION

We have conducted molecular dynamics simulations of polybutadiene (PBD) melts using a chemically realistic united atom model. Despite the fact that the model [24, 26] is well established and has been extensively employed in studies of bulk melts [4, 24, 26–30] and polymer films [31–35], the present paper begins with a detailed description of the model. There are two reasons for this. First, since its introduction the model has undergone several changes. In particular, recent simulations with the GROMACS code [31–35] used an adapted version of the original potential functions. Therefore, it seems helpful to gather the information about the potentials from these different sources for later reference. Second, we have changed the potentials for the bond length and Lennard–Jones (LJ) pair interactions. The original model [24, 26] used rigid bonds and truncated LJ potentials with tail corrections. Instead of this, we utilize harmonic bond potentials and pair interactions that ensure continuity of the potential up to the second derivative at the cutoff distance. Although there are theoretical arguments that flexible bonds are a more accurate than rigid bonds when treating chain conformations by classical statistical mechanics [105], our choice not to fix the bond length is mainly motivated by the fact that the simulations have been carried out with the LAMMPS code which does not support, contrary to GROMACS, the constraint of rigid bonds for polymers. For the pair interactions, our choice of ensuring continuity of the potential up to the second derivative has the advantage of avoiding impulsive corrections [45, 46], which otherwise need to be taken into account e.g. in the computation of elastic constants [106–108]. This amendment of the model may therefore be helpful when extending future studies to the elasticity of polymer glasses. The parameters of our modified force field have been adapted so as to reproduce key properties of the original PBD model. In this way, we keep the salient features of the original model, while rendering it at the same time more versatile through the amendments proposed here.

Prompted by studies of the original PBD model [19–22] and other polymers [5, 17, 18] the present work focuses on the influence that reduction or elimination of the dihedral potentials has on chain conformations, basic thermodynamic properties and glass transition, if all other potentials are kept the same. For the equilibrium polymer liquid we find that the impact of the dihedrals on chain conformations is weak. Even when eliminating all torsional potentials the chains become only slightly more flexible (Table V and Fig. 8). This remarkable observation agrees with the original work of Refs. [19, 20]; it implies that an important contribution to chain stiffness in PBD stems from local correlations involving four or more bonds along the chain backbone. The weak influence of the dihedral potentials on chain conformations is in stark contrast to their strong impact on dynamic properties. Prior work with the original model [19–22] reported a significant enhancement of the local and polymer dynamics when reducing or eliminating the dihedral potentials. This result resonates with studies of other polymer models [5, 17, 18] and our finding that $T_{\rm g}$ decreases by about 150 K when going from the CRC model with full torsional potential to the FRC model with no torsional potential (Table VI and Fig. 9).

While we do not anticipate that the dichotomy of the influence of the dihedral potential—weak effect on chain conformations, huge impact on dynamics—is generally valid, it is an attractive feature of the PBD model, which could be harnessed in polymer glass simulations. One can imagine to design a model that maintains the potential wells of the dihedrals but reduces the barriers so as to promote "tunneling" between the wells. Ideally, such a model would only speed up the dynamics without changing static properties of the underlying CRC model. In this way, equilibration could be achieved at temperatures where relaxation times for standard MD would be

prohibitively large for current computational resources.

We have also investigated the T dependence of the density ρ and isothermal compressibility κ_T in the equilibrium polymer liquid. In excellent approximation, we find ρ and κ_T to be independent of the torsional potentials (Fig. 11). This finding may be rationalized as follows: As shown in Ref. [109], the virial equation for the pressure does not depend explicitly on angular bending and dihedral potentials. These potentials only enter implicitly, through thermal averaging of the virial for the bond-length and pair potentials. But now the bond length is a hard variable, essentially decoupled from the other variables and so from the torsional potential in the polymer liquid (Fig. 12). Therefore, the virial of the bond-length potential is (virtually) independent of the torsions. The virial of the pair potential is determined by the intramolecular and intermolecular pair-correlation functions [109]. We find (not shown here) that the influence of dihedrals on intermolecular pair correlations is very weak, while it is a bit stronger for intramolecular correlations, but mainly for distances between united atoms that have no pair interactions along the chain backbone. Therefore, also the virial of the pair potential is essentially independent of the torsions. These arguments together explain why density and related quantities, such as κ_T, are not coupled to the strength of the dihedral potentials for our PBD model.

Schweizer and coworkers have recently discovered that nonpolar molecular and polymer liquids obey a linear scaling relation between $1/\sqrt{k_\mathrm{B}T\rho\kappa_T}$ and $1/T$ and rationalized this result by the van–der–Waals (vdW) equation of state [84–86]. We verified that this linear scaling works very well for our PBD model (Fig. 11). A vdW model, similar to one discussed in Refs. [84–86], has been proposed before by Long and Lequeux [90, 92]. We find that the Long–Lequeux model provides a very good fit of both κ_T and ρ (Fig. 11), and also gives back the linear scaling of $1/\sqrt{k_\mathrm{B}T\rho\kappa_T}$ with $1/T$ in the low-T limit. The T range of applicability of the Long–Lequeux model could thus be larger and might help explain the deviations from the linear scaling observed in recent simulations of coarse-grained polymer models at high T [7]. Although the Long–Lequeux model allows to parameterize the T dependence of ρ and κ_T for our model, this does not exclude that alternative approaches, based e.g. on generalized entropy [7, 8] or advanced free volume [110] concepts, can also provide a consistent description of the data.

Another key thermodynamic quantity is the specific heat at constant pressure c_p or at constant volume c_V. By definition, reduction or elimination of the torsional potentials must have a pronounced impact on the specific heat. We illustrate this impact for c_p in Fig. 16 and find for all models that c_p increases with decreasing T. Decomposition of c_p into the different energetic contributions reveals that the T dependence stems from anharmonic terms in the dihedral energy and from the LJ energy (Fig. 17), the latter being very well described by the functional form proposed by Rosenfeld and Tarazona [94, 96] (Fig. 15). The increase of c_p or c_V (Fig. 17) upon cooling is, however, opposite to the T dependence found in experiment for many liquid polymers [3, 101], including PBD [100]. Since the results obtained by the CRC model for other static (cf. Sec. III B and Sec. IV and also [4, 24, 26]) or dynamic properties [4, 27–30] are in good agreement with experiment, the difference for the specific heat, shown in the inset of Fig. 17, is surprising. We argue that this difference is a consequence of the classical united atom model chosen for PBD, which misses, by construction, quantum mechanical effects due to hydrogen atoms and backbone vibrations. In hindsight, such quantum effects must have been expected on the basis of the comprehensive work by Wunderlich and coworkers [101]. The importance of quantum effects for the modeling of the specific heat is also pointed out in other recent studies [103, 111]. While quantum mechanics is thus pertinent for a realistic description of hydrogen atoms and backbone vibrations, these degrees of freedom are not coupled (or only very weakly) to the density of PBD or other polymers, the temperature dependence of which may be modeled accurately by approaches based on classical statistical mechanics, such as the Long–Lequeux model [90, 92] or recent extensions of free-volume theory [110].

In the future we plan to extend our studies to the equilibrium dynamics of PBD melts. Based on the changes of T_g observed here and prior work with the original model [19–22], we expect that reduction or elimination of the dihedral potentials accelerate the local dynamics. It is plausible that this effect is present at all temperatures. At high T, it is often found that the α relaxation time τ_α exhibits an Arrhenius behavior, $\tau_\alpha \propto \exp(E_\mathrm{A}/k_\mathrm{B}T)$ with E_A being the activation energy [8, 84, 112]. Acceleration of the dynamics should be reflected by a decrease of E_A when going from the CRC model with full torsional potential to the FRC model with no torsional potential. On approach to T_g the activation barrier increases with decreasing T. The changes of T_g reported here suggest that this low-T barrier also decreases with reduction of the torsional potentials. Since our PBD models with modified dihedral potentials affect only very weakly chain conformations, the ensemble averaged static structure factor of the melt, and thermodynamic properties related to the density, a systematic study of the impact of dihedral barriers on the equilibrium dynamics may be of fundamental importance: on the one hand, for developing theories that posit a causal relationship between these equilibrium static properties and polymer glass formation, and on the other hand, for structure based coarse-graining approaches that map bead-spring models to real polymers [113] and for which the static Kuhn length as a coarse-graining scale might not necessarily faithfully represent the dynamic size of a bead [114].

SUPPLEMENTARY MATERIAL

The supplemental material provides further information about the model and simulation, the fits of bond-correlation function and internal distances to the freely-rotating-chain-model theory, the fits of the T dependence of the density from the continuous cooling runs, the fits of the density and compressibility to the Long–Lequeux model, and the fits of the T dependence of the different contributions to the potential energy. Tables summarize the results for the fit parameters.

ACKNOWLEDGMENTS

We are very grateful to G.B. McKenna for several helpful discussions, in particular on the specific heat. F.D. acknowledges funding from the Excellence Initiative (IdEx) of the University of Strasbourg. Our simulation work was made possible by a generous grant of computer time at the High Performance Computing (HPC) Center of the University of Strasbourg and on the Jean Zay (HPE SGI 8600) supercomputer at the Institute for Development and Resources in Intensive Scientific Computing (IDRIS, Orsay).

[1] C. A. Angell, K. L. Ngai, G. B. McKenna, P. F. McMillan, and S. W. Martin, J. Appl. Phys. **88**, 3113 (2000).
[2] L. Berthier and G. Biroli, Rev. Mod. Phys. **83**, 587 (2011).
[3] G. B. McKenna and S. L. Simon, Macromolecules **50**, 6333 (2017).
[4] W. Paul and G. D. Smith, Rep. Prog. Phys. **67**, 1117 (2004).
[5] J. Colmenero, J. Phys.: Condens. Matter **27**, 103101 (2015).
[6] J. H. Gibbs and E. A. DiMarzio, J. Chem. Phys. **28**, 373 (1958).
[7] W.-S. Xu, J. F. Douglas, and X. Xu, Macromolecules **53**, 9678 (2020).
[8] W.-S. Xu, J. F. Douglas, and Z.-Y. Sun, Macromolecules **54**, 3001 (2021).
[9] S. Mirigian and K. S. Schweizer, Macromolecules **48**, 1901 (2015).
[10] S.-J. Xie and K. S. Schweizer, Macromolecules **49**, 9655 (2016).
[11] S.-J. Xie and K. S. Schweizer, Macromolecules **53**, 5350 (2020).
[12] A. Arbe, F. Alvarez, and J. Colmenero, Polymers **12**, 3067 (2020).
[13] J. Baschnagel, I. Kriuchevskyi, J. Helfferich, C. Ruscher, H. Meyer, O. Benzerara, J. Farago, and J. Wittmer, in *Polymer Glasses*, edited by C. B. Roth (CRC Press, Taylor & Francis Group, 2016) Chap. 3.
[14] J.-H. Hung, T. K. Patra, V. Meenakshisundaram, J. H. Mangalara, and D. S. Simmons, Soft Matter **15**, 1223 (2019).
[15] W.-S. Xu, J. F. Douglas, and X. Xu, Macromolecules **53**, 4796 (2020).
[16] M. Bernabei, A. J. Moreno, and J. Colmenero, Phys. Rev. Lett. **101**, 255701 (2008).
[17] M. Bernabei, A. J. Moreno, and J. Colmenero, J. Chem. Phys. **131**, 204502 (2009).
[18] M. Bernabei, A. J. Moreno, E. Zaccarelli, F. Sciortino, and J. Colmenero, J. Chem. Phys. **134**, 024523 (2011).
[19] S. Krushev, W. Paul, and G. D. Smith, Macromolecules **35**, 4198 (2002).
[20] S. Krushev and W. Paul, Phys. Rev. E **67**, 021806 (2003).
[21] D. Bedrov and G. D. Smith, Phys. Rev. E **71**, 050801 (2005).
[22] G. D. Smith and D. Bedrov, J. Polym. Sci. Part B: Polym. Phys. **45**, 627 (2007).
[23] P. J. Flory, *Statistical Mechanics of Chain Molecules* (Wiley, New York, 1969).
[24] G. D. Smith and W. Paul, J. Phys. Chem. A **102**, 1200 (1998).
[25] Following earlier work [4, 24, 35] no distinction is made between inner and end monomers, i.e. the CH_3 group at the chain end is replaced by a CH_2 group for computational convenience.
[26] G. D. Smith, W. Paul, M. Monkenbusch, D. Richter, X. H. Qiu, and M. D. Ediger, Macromolecules **32**, 8857 (1999).
[27] O. Byutner and G. D. Smith, Macromolecules **34**, 134 (2001).
[28] O. Byutner and G. D. Smith, Macromolecules **35**, 3769 (2002).
[29] G. D. Smith, W. Paul, M. Monkenbusch, and D. Richter, J. Chem. Phys. **114**, 4285 (2001).
[30] G. D. Smith, O. Borodin, and W. Paul, J. Chem. Phys. **117**, 10350 (2002).
[31] L. Yelash, P. Virnau, K. Binder, and W. Paul, Europhys. Lett. **98**, 28006 (2012).
[32] M. Solar, E. U. Mapesa, F. Kremer, K. Binder, and W. Paul, Europhys. Lett. **104**, 66004 (2013).
[33] M. Solar and W. Paul, Eur. Phys. J. E **38**, 37 (2015).
[34] M. Solar, K. Binder, and W. Paul, J. Chem. Phys. **146**, 203308 (2017).
[35] M. Solar and W. Paul, in *The Scaling of Relaxation Processes*, Advances in Dielectrics, edited by F. Kremer and A. Loidl (Springer, Berlin, Heidelberg, New York, 2018) pp. 353–374.
[36] GROMACS (GROningen MAchine for Chemical Simulation), http://www.gromacs.org/. Documentation available at https://doi.org/10.5281/zenodo.4723561.

[37] W. Paul, D. Bedrov, and G. D. Smith, Phys. Rev. E **74**, 021501 (2006).

[38] LAMMPS (Large-scale Atomic/Molecular Massively Parallel Simulator), http://lammps.sandia.gov.

[39] P. Nallasamy, P. M. Anbarasan, and S. Mohan, Turkish Journal of Chemistry **26**, 105 (2002).

[40] To get Eq. (3) we insert the identity $\cos\theta - \cos\theta_0 = -2\sin[(\theta+\theta_0)/2]\sin[(\theta-\theta_0)/2]$ into Eq. (2) and assume deviations of θ from θ_0 to be small.

[41] J.-P. Ryckaert and A. Bellemans, Chem. Phys. Lett. **30**, 123 (1975).

[42] See Supplemental Material for further details.

[43] We utilize the value of Boltzmann constant defined in the LAMMPS code, $k_{\rm B} = 0.001\,987\,2067$ kcal/(mol K).

[44] M. Rubinstein and R. H. Colby, *Polymer Physics* (Oxford University Press, Oxford, 2003).

[45] D. Frenkel and B. Smit, *Understanding Molecular Simulation*, 2nd ed. (Academic Press, London, 2002).

[46] H. Xu, J. P. Wittmer, P. Polińska, and J. Baschnagel, Phys. Rev. E **86**, 046705 (2012).

[47] J. P. Hansen and I. R. McDonald, *Theory of Simple Liquids* (Academic Press, London, 1986).

[48] A. Ninarello, L. Berthier, and D. Coslovich, Phys. Rev. X **7**, 021039 (2017).

[49] T. S. Ingebrigtsen, J. C. Dyre, T. B. Schrøder, and C. P. Royall, Phys. Rev. X **9**, 031016 (2019).

[50] W. Kob and H. C. Andersen, Phys. Rev. E **51**, 4626 (1995).

[51] W. Kob and H. C. Andersen, Phys. Rev. E **52**, 4134 (1995).

[52] D. Coslovich, M. Ozawa, and W. Kob, Eur. Phys. J. E **41**, 62 (2018).

[53] B. Schnell, H. Meyer, C. Fond, J. Wittmer, and J. Baschnagel, Eur. Phys. J. E **34**, 97 (2011).

[54] D. Bedrov and G. D. Smith, J. Non-Cryst. Solids **357**, 258 (2011).

[55] S. C. Plimpton, Comput. Phys. **117**, 1 (1995).

[56] We estimate the bond oscillation time $\tau_{\rm bond}$ as the period of a bond oscillation associated with the CH group, i.e. with the united atom that has the smallest mass: $\tau_{\rm bond} = 2\pi\sqrt{m_{\rm CH}/(2K_{\rm bond})} \approx 1.6\times10^{-14}$ s with 1 kcal/mol = 4184 J/mol. The LJ time scale associated with the pair interactions of the CH group is much larger: $\tau_{\rm LJ} = (m_{\rm CH}\sigma^2_{\rm CH,CH}/\epsilon_{\rm CH,CH})^{1/2} \approx 1.8\times10^{-12}$ s.

[57] In experiments typical cooling rates are $\Gamma = 10^{-3}$-10^{0} K/s [58, 73, 115], while in simulations the rates are in the range 10^{9}-10^{12} K/s [13, 116]. Our cooling rate, $\Gamma = 0.83\,{\rm K/ns} = 8.3\times10^{8}$ K/s, is thus at the lower bound of the values employed in simulations.

[58] A. L. Agapov and A. P. Sokolov, Macromolecules **42**, 2877 (2009).

[59] J. Hintermeyer, A. Herrmann, R. Kahlau, C. Goiceanu, and E. A. Rössler, Macromolecules **41**, 9335 (2008).

[60] The idea that the torsional potential could have only a perturbative influence on the pressure was spurred by the work of Honnell *et al.* on the virial expression for p [109], showing that the virial contributions of the bond and torsional angles vanish. We verified this prediction by our simulations. Moreover, as a further check we started NPT simulations at $p = 0$ atm from the final NVT configuration of the production run for all models. The densities determined from these NPT runs agree within 0.5% with those imposed in the NVT runs.

[61] A. N. Semenov, Macromolecules **43**, 9139 (2010).

[62] J. P. Wittmer, P. Beckrich, H. Meyer, A. Cavallo, A. Johner, and J. Baschnagel, Phys. Rev. E **76**, 011803 (2007).

[63] J. P. Wittmer, H. Meyer, J. Baschnagel, A. Johner, S. Obukhov, L. Mattioni, M. Müller, and A. N. Semenov, Phys. Rev. Lett. **93**, 147801 (2004).

[64] H.-P. Hsu and K. Kremer, J. Chem. Phys. **144**, 154907 (2016).

[65] C. Svaneborg and R. Everaers, Macromolecules **53**, 1917 (2020).

[66] M. Doi and S. F. Edwards, *The Theory of Polymer Dynamics* (Oxford University Press, Oxford, 1986).

[67] L. J. Fetters, D. J. Lohse, and R. H. Colby, in *Physical Properties of Polymers Handbook*, edited by J. E. Mark (Springer, New York, 2007) p. 447.

[68] The stiff bond length potential of the PBD model implies that the bond length is Gaussian distributed around the equilibrium bond length ℓ_0, leading to a T independent $\langle\vec{\ell}^{\,2}\rangle = \ell_0^2$. Out of $N-1$ bonds, a PBD chain has $N/4$ CH=CH bonds of length $\ell_0 = 1.34$ Å, $N/4-1$ CH_2–CH_2 bonds of length $\ell_0 = 1.53$ Å, and $N/2$ CH–CH_2 bonds of length $\ell_0 = 1.50$ Å. The arithmetic mean of these three contributions gives $l^2 = 2.158\,{\rm Å}^2$.

[69] J. W. Mays, N. Hadjichristidis, W. W. Graessley, and L. J. Fetters, J. Polym. Sci. B **24**, 2553 (1986).

[70] Y. Abe and P. J. Flory, Macromolecules **4**, 219 (1971).

[71] G. B. McKenna, in *Comprehensive Polymer Science*, Vol. 2, edited by C. Booth and C. Price (Pergamon, New York, 1986) pp. 311–362.

[72] C. M. Roland, S. Hensel-Bielowka, M. Paluch, and R. Casalini, Rep. Prog. Phys. **68**, 1405 (2005).

[73] J. M. Caruthers and G. A. Medvedev, in *Polymer Glasses*, edited by C. B. Roth (CRC Press, Taylor & Francis Group, 2016) Chap. 4.

[74] J. Buchholz, W. Paul, F. Varnik, and K. Binder, J. Chem. Phys. **117**, 7364 (2002).

[75] K. Vollmayr, W. Kob, and K. Binder, J. Chem. Phys. **54**, 15808 (1996).

[76] A. V. Lyulin, B. Vorselaars, M. A. Mazo, N. K. Balabaev, and M. A. J. Michels, Europhys. Lett. **71**, 618 (2005).

[77] K. Dalnoki-Veress, J. A. Forrest, C. Murray, C. Gigault, and J. R. Dutcher, Phys. Rev. E **63**, 031801 (2001).

[78] G. D. Smith, O. Borodin, D. Bedrov, W. Paul, X. Qiu, and M. D. Ediger, Macromolecules **34**, 5192 (2001).

[79] R. H. Colby, L. J. Fetters, and W. W. Graessley, Macromolecules **20**, 2226 (1987).

[80] H. B. Callen, *Thermodynamics and an Introduction to Thermostatistics* (Wiley, New York, 1985).

[81] J. L. Lebowitz, J. K. Percus, and L. Verlet, Phys. Rev. **153**, 250 (1967).

[82] J. P. Wittmer, H. Xu, P. Polińska, F. Weysser, and J. Baschnagel, J. Chem. Phys. **138**, 191101 (2013).

[83] K. S. Schweizer and E. J. Saltzman, J. Chem. Phys. **121**, 1984 (2004).

[84] S. Mirigian and K. S. Schweizer, J. Chem. Phys. **140**, 194507 (2014).

[85] B. Mei, Y. Zhou, and K. S. Schweizer, (preprint).

[86] B. Mei, Y. Zhou, and K. S. Schweizer, PNAS **118**, e2025341118 (2021).

[87] S. Mirigian and K. S. Schweizer, J. Chem. Phys. **146**, 203301 (2017).

[88] A. D. Phan and K. S. Schweizer, Macromolecules **51**, 6063 (2018).

[89] K. S. Schweizer and D. S. Simmons, J. Chem. Phys. **151**, 240901 (2019).

[90] D. Long and F. Lequeux, Eur. Phys. J. E **4**, 371 (2001).

[91] I. Prigogine, *The Molecular Theory of Solutions* (North-Holland, Amsterdam, 1957).

[92] E. M. Masnada, G. Julien, and D. Long, J. Polym. Sci. B **52**, 419 (2014).

[93] F. Sciortino, J. Stat. Mech. **5**, P05015 (2005).

[94] Y. Rosenfeld and P. Tarazona, Mol. Phys. **95**, 141 (1998).

[95] M. Baggioli and A. Zaccone, Phys. Rev. E **104**, 014103 (2021).

[96] T. S. Ingebrigtsen, A. A. Veldhorst, T. B. Schrøder, and J. C. Dyre, J. Chem. Phys. **139**, 171101 (2013).

[97] T. S. Ingebrigtsen, T. B. Schrøder, and J. C. Dyre, Phys. Rev. X **2**, 011011 (2012).

[98] The enthalpy $H(\boldsymbol{x}) = \mathcal{H}(\boldsymbol{x}) + pV(\boldsymbol{x})$ depends on the microstate $\boldsymbol{x}$ of the system. The specific heat is given by $c_p = (\langle H^2\rangle - \langle H\rangle^2)/N_\mathrm{c}Nk_\mathrm{B}T^2$. Since the NPT simulations were carried out at $p = 0$ pressure, we have $H(\boldsymbol{x}) = \mathcal{H}(\boldsymbol{x})$ and c_p can be calculated from the fluctuations of the hamiltonian $\mathcal{H}$ only.

[99] Here we assume that the number of degrees of freedom is $g = 3N_\mathrm{c}N$, while $g = 3(N_\mathrm{c}N - 1)$ from the thermodynamic output provided by LAMMPS (docs.lammps.org/compute_ke.html) because the center-of-mass velocity of the system is set to 0. As $N_\mathrm{c}N = 4640$ for our system, the difference between $N_\mathrm{c}N$ and $N_\mathrm{c}N - 1$ can be neglected.

[100] J. Grebowicz, W. Aycock, and B. Wunderlich, Polymer **27**, 575 (1986).

[101] B. Wunderlich, *Thermal Analysis of Polymeric Materials* (Springer, Berlin–Heidelberg, 2005).

[102] M. Pyda and B. Wunderlich, Macromolecules **32**, 2044 (1999).

[103] H. Gao, T. P. W. Menzel, M. H. Müser, and D. Mukherji, Phys. Rev. Mater. **5**, 065605 (2021).

[104] R. Martoňák, W. Paul, and K. Binder, Phys. Rev. E **57**, 2425 (1998).

[105] N. Gō and H. A. Scheraga, Macromolecules **9**, 535 (1976).

[106] J. P. Wittmer, H. Xu, P. Polińska, F. Weysser, and J. Baschnagel, J. Chem. Phys. **138**, 12A533 (2013).

[107] I. Kriuchevskyi, J. P. Wittmer, H. Meyer, O. Benzerara, and J. Baschnagel, Phys. Rev. E **97**, 012502 (2018).

[108] L. Klochko, J. Baschnagel, J. P. Wittmer, and A. N. Semenov, Soft Matter **17**, 7867 (2021).

[109] K. G. Honnell, C. K. Hall, and R. Dickman, J. Chem. Phys. **87**, 664 (1987).

[110] R. P. White and J. E. G. Lipson, Macromolecules **49**, 3987 (2016).

[111] D. Bolmatov, V. V. Brazhkin, and K. Trachenko, Sci. Rep. **2**, 421 (2012).

[112] B. Schmidtke, M. Hofmann, A. Lichtinger, and E. A. Rössler, Macromolecules **48**, 3005 (2015).

[113] R. Everaers, H. A. Karimi-Varzaneh, F. Fleck, N. Hojdis, and C. Svaneborg, Macromolecules **53**, 1901 (2020).

[114] A. Agapov and A. P. Sokolov, Macromolecules **43**, 9126 (2010).

[115] R. Brüning and K. Samwer, Phys. Rev. B **46**, 11318 (1992).

[116] A. V. Lyulin, N. K. Balabaev, and M. A. J. Michels, Macromolecules **36**, 8574 (2003).